REPORT DOCUMENTATION PAGE

Public reporting burden for this collection of information is estimated to average 1 hour per response, including the time for reviewing instructions, searching existing data sources, gathering and maintaining the data needed, and completing and reviewing this collection of information. Send comments regarding this burden estimate or any other aspect of this collection of information, including suggestions for reducing this burden to Department of Defense, Washington Headquarters Services, Directorate for Information Operations and Reports (0704-0188), 1215 Jefferson Davis Highway, Suite 1204, Arlington, VA 22202-4302. Respondents should be aware that notwithstanding any other provision of law, no person shall be subject to any penalty for failing to comply with a collection of information if it does not display a currently valid OMB control number. **PLEASE DO NOT RETURN YOUR FORM TO THE ABOVE ADDRESS.**

1. REPORT DATE *(DD-MM-YYYY)* 29-02-2012	2. REPORT TYPE Final Report	3. DATES COVERED *(From - To)* Mar 2009 - Nov 2011	
4. TITLE AND SUBTITLE NANOENGINEERING TESTBED FOR NANOSOLAR CELL AND PIEZOELECTRIC COMPOUNDS		**5a. CONTRACT NUMBER**	
		5b. GRANT NUMBER FA9550-09-1-0268	
		5c. PROGRAM ELEMENT NUMBER	
6. AUTHOR(S) Shen, Yin-Lin		**5d. PROJECT NUMBER**	
		5e. TASK NUMBER	
		5f. WORK UNIT NUMBER	
7. PERFORMING ORGANIZATION NAME(S) AND ADDRESS(ES) George Washington University 2121 Eye Street, NW Washington, DC 20052		**8. PERFORMING ORGANIZATION REPORT NUMBER**	
9. SPONSORING / MONITORING AGENCY NAME(S) AND ADDRESS(ES) Air Force Office of Scientific Research 875 North Randolph Street Suite 325, Rm 3112 Arlington, VA 22203		**10. SPONSOR/MONITOR'S ACRONYM(S)** AFOSR	
		11. SPONSOR/MONITOR'S REPORT NUMBER(S) AFRL-OSR-VA-TR-2012-0525	

12. DISTRIBUTION / AVAILABILITY STATEMENT

A

13. SUPPLEMENTARY NOTES

14. ABSTRACT

This project designed nanoscale solar voltaic cells by using carbon nanotubes. The Field-Effect Transistor of canbon nanotube was adopted and asymmetric Schottky barriers made of two different metal-semiconductor barriers at both ends of carbon nanotubes were employed to enhance the Einstein photoelectric electron-hole separation. Two architectures of the nanoscale solar cell were designed and analyzed.

This project also examined the use of finite element analysis to simulate the process of nanoindentation to gain insights into the behavior of elastoplastic and viscoelastic materials. The study examined the behavior of a calibrated elastoplastic material model during indentations using different indenter tip geometries. The study then compared simulations and experimental results for the elastoplastic material. Additionally, the study examined the calibration of a viscoelastic material model from reported data and its ability to predict indentation response.

15. SUBJECT TERMS

16. SECURITY CLASSIFICATION OF:			**17. LIMITATION OF ABSTRACT**	**18. NUMBER OF PAGES**	**19a. NAME OF RESPONSIBLE PERSON**
a. REPORT	**b. ABSTRACT**	**c. THIS PAGE**			**19b. TELEPHONE NUMBER** *(include area code)*

Final Performance Report

Project title:

Nanoengineering Testbed for Nanosolar Cell and Piezoelectric Compounds

Grant Number: FA9550-09-1-0268

Program manager: Dr. Kitt Reinhardt, AFOSR

Yin-Lin Shen, Ph.D. and Professor

Mechanical and Aerospace Engineering Department

George Washington University

Feb. 29, 2012

Abstract

This project designed nanoscale solar voltaic cells by using carbon nanotubes. The Field-Effect Transistor of canbon nanotube was adopted and asymmetric Schottky barriers made of two different metal-semiconductor barriers at both ends of carbon nanotubes were employed to enhance the Einstein photoelectric electron-hole separation. Two architectures of the nanoscale solar cell were designed and analyzed. This project also examined the use of finite element analysis to simulate the process of nanoindentation to gain insights into the behavior of elastoplastic and viscoelastic materials. The study examined the behavior of a calibrated elastoplastic material model during indentations using different indenter tip geometries. The study then compared simulations and experimental results for the elastoplastic material. Additionally, the study examined the calibration of a viscoelastic material model from reported data and its ability to predict indentation response.

I. Summary of work in nano scale solar voltaic cells by using carbon nano tubes

I.1 Introduction

Shockley and Queisser have computed in 1961 the upper limit of 30% converting 1000 Watts/m^2 sun to 300 Watts/m^2 of any Schottky semiconductor, e.g., silicon p-n junction device at the band gap at 1.1 eV as discovered by Bell Lab in 1954; and such a solar battery, installed by Hoffman electronics, on board of US Satellite Vanguard 1, 1958. The upper limit is due to photo-excitation mechanism which must be above the Fermi level of the silicon or the GaAs semiconductor band gap at 1.1 eV or 1.52 eV respectively, which excludes the long infrared, microwaves, radio, except visible photons to generate free conduction band electrons. In this project, we explored Carbon NanoTubes (CNT) technology to break the Shockley-Queisser theoretical barriers of visible-only solar cells. We adopted the simple spherical camera lens which is made of Pb-Crown glass of F#=0.7 af the Lens$_{diameter}$=2cm, which will provide a uniform focusing of sunlight, from the visible to near infrared (NIR), up to millions times stronger upon at the yellow-light focal plane, enjoying the maximum-number of photons.

I.2 Design of voltaic solar cells using carbon nanotubes

The diameter of lenslet array was chosen as 2 cm and the lenslet was made of Pb-lead-Crown glass with the refractive index around 1.52 and F# is 0.7, focusing the maximum number of photons in the visible yellow 0.635 μm and red 0.73 μm, at the sharpest Rayleigh diffraction-limit spot size yellow-light focal plane. Thus, judging from the Planck

radiation spectrum shape equivalent to the sun at 6000 °K (peak at Yellow) ~5000 °K (peak at Red), without the atmosphere in the space, the visible band was considered from 0.4μm to 0.73μm, and the infrared band from 0.73 μm to 1.12 μm being limited by the Pb-Crown glass flat transmission. Then, thermal re-remittance loss due to a hot solar panel had been considered to be negligibly small percentage by Landsberg and Baruch. Furthermore, we realized the band gap concept of semiconductor to be a lower threshold of minimum photon energy to excite conduction charge carriers, and thus we chose a relatively larger cross-section and lower band-gap threshold active element. It turns out to be the near infrared at 1.12 μm and Carbon NanoTube (CNT) with the diameter of 0.66 nm. The focal plane was chosen for Yellow-light at the Rayleigh diffraction limit spot size, which had the maximum number of photons concentrated at the focal plane.

Mosaic solar panel at the size of 2m by 2m could be made manageable to a Space-Robotic, e.g. Canadian arm. It was packed with 100x100 unit volume cells, as shown in Figure 1.

$$F\# = z/D_{lens} = 0.7 \tag{1}$$

$$A_{lens} = \pi \cdot r^2 = \pi \, (0.01\text{m})^2 = 0.000314\text{m}^2 = \pi \text{ cm}^2 \tag{2}$$

$$active \; Fill \; Factor_{Panel} = \frac{honey - comb \; lenselet \; collector}{Squared \; Frame \; Panel}$$

$$= \frac{N \times M \times \pi \cdot r^2}{[(r(N-1)\sqrt{3} + 2r) \cdot (2M + 1)r]} = \frac{N \times M \times \pi}{[(\sqrt{3}N + 2 - \sqrt{3}) \cdot (2M + 1)]} \tag{3}$$

When N and M become very large, the solar-Active Factor panel is near a constant of $\pi/2 \cdot 3^{1/2} \approx 90\%$. Thus, the total solar energy is at most reduced by 10% frame boundary used to hold the lenslet array in to the firm place.
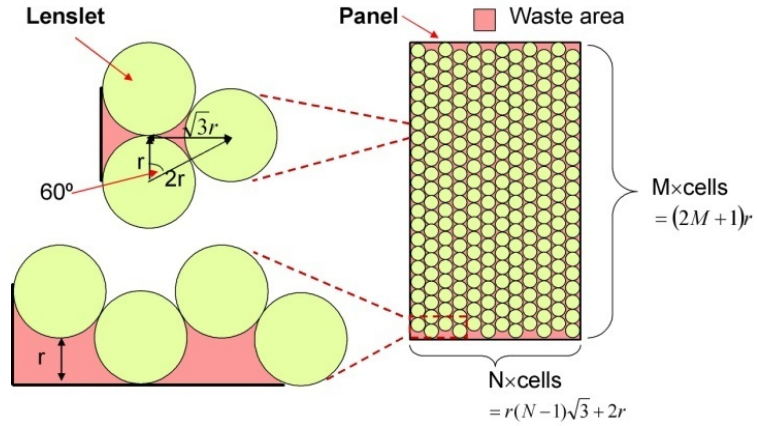
Figure 1. Solar cells fill in a percentage of the panel Crown glass is type of optical glass used in lenses and other optical components. Crown glass is produced from alkali-lime (RCH) silicates containing refractive index ($\approx$1.52) and low dispersion

In order to estimate the relative output electric power based on our several design architectures, we could fix the common microscopic parameters, such as the photoelectric surface work potential function $W_{Einstein}$ and the difference effect of asymmetric potential barriers $\Phi_{Schottky}$ at both ends, as well as the Einstein photoelectric conversion efficiency, $\eta_{Einstein}$ of CNTs and the carrier transport collision extinction $Ex_{collision}$(to be optimized by our subsequent kinetic R/D). In a unit cell system, the focus plane was generally chosen at the visible yellow light in favor of generating a higher velocity V_{vis} of the electrical charge

carrier which contribute to a larger photo-electric current using the justifiable classical and semi-classical formulae:

$$I_{vis} \cong q\, N_e\, V_{vis}. \tag{4}$$

$$\frac{1}{2} m_e V_{vis}^2 = \hbar\omega_{vis} - qW_{Einstein} + q\Phi_{Shockley} \cong \hbar\omega_{vis} \tag{5}$$

$$V_{yellow} = 8.2\times 10^5 \text{m/s}, \quad V_{NIR} = 6.2\times 10^5 \text{m/s} \tag{6}$$

In our design we approximated the integrated majority yellow photon visible band at a typical yellow light and the Crown-glass-passable near infrared light NIR as follows:

$$\lambda_{yellow} \cong 0.635\mu\text{m}, \; E_{yellow} = 1.26\times 10^2 \text{ J/(s·m}^2), \; \omega_{yellow} = 2.97\times 10^{15} \text{rad/s} \tag{7}$$

and for NIR light

$$\lambda_{IR} \cong 1.12\mu\text{m}, \; E_{IR} = 78 \text{ J/(s m}^2), \; \omega_{IR} = 1.68\times 10^{15} \text{ rad/s} \tag{8}$$

A more photon collector in a larger CNT diameter associated with infrared (IR) photons according to Seito band gap relation:

$$E_{Saito\ BG} = \frac{2\gamma_0 \cdot a_{CC}}{d_{CNT}} \; , \; E_{Einstein} = hc/\lambda = (1.24 \text{ eV})/(\lambda\ \mu\text{m}) \tag{9}$$

6

where a_{C-C} is 1.41Å, neighborhood hoping distance, γ_0 =2.6 eV= energy of neighborhood hopping interaction.

We chose

$$d_{CNT}(\lambda_{NIR})= 0.66 \text{ nm}; \quad E_{BG}(NIR)=1.107 \text{ eV} \tag{10}$$

The band gap formula in Equation 9 was verifiable because of the transitional regime permitted a mixed treatment of classical physics and quantum mechanics. The propagating electron along CNT whose quantum mechanical de Broglie wavelength going around the circumference of CNT was computed as Sommerfeld-Bohr quantization condition as an integer of the circumference as follows:

$$\lambda_{De\,Boglie} = \frac{h}{P_{electron}} = n\,\pi\,d_{CNT}(\lambda_{NIR}) \quad ; \quad \text{n=1,2, etc.} \tag{11}$$

de Broglie matter wave going around single layer of CNT lattice equals once to be in phase with itself for n=1 for NIR, and then for n=2 twice for the visible red.

Because of a larger basket can catch both the smaller visible photons generating larger kinetic velocity of the charge carriers and the larger NIR photons generating smaller kinetic velocity of the charge carriers, according to the semiconductor Femi level at NIR band gap. However, whenever possible, we chose the focal length to be located at the Lord Rayleigh

diffraction limit smallest spot size at the shorter yellow wavelength where an abundance of solar photons existed, and produces larger velocity charge carriers than NIR.

We suppose that all 16 NIR-CNTs may be spirally packaged in the Rayleigh yellow-light focusing origin, of which the central core thickness becomes increased linearly from 0.66nm to 0.66x16=10.56nm, where the diffraction-limited spot size was de-focused from for NIR.

Given the common material constants in MKS units adopted by solar energy community:

$$m_e = 9.11 \times 10^{-31} \text{ Kg}, \hbar = 1.054 \times 10^{-34} \text{ J·s}, q = -1.602 \times 10^{-19} \text{ Coulomb} \quad (12)$$

We computed the total number of photons involved in photoelectric conversion by the following conservation of energy formula

$$Total\_Energy \ (shorter \ \& \ including \ \lambda)$$

$$= E_\lambda \cdot A_{Lens} \cdot \frac{A_{CNTs}}{A_{SpotSize}} = N_{photon} \cdot \hbar \cdot \omega \quad (13)$$

$$N_{photon\_yellow} = E_{yellow} \cdot A_{Lens} \cdot \frac{A_{CNTs}(\lambda_{yellow})}{A_{SpotSize}(\lambda_{yellow})} / \hbar \cdot \omega_{yellow}$$

$$= 5.44 \times 10^{16} \quad (14)$$

$$N_{photon\_NIR} = E_{NIR} \cdot A_{Lens} \cdot \frac{A_{CNTs}(\lambda_{NIR})}{A_{SpotSize}(\lambda_{NIR})} / \hbar \cdot \omega_{NIR} \cong 1.89 \times 10^{15} \quad (15)$$

We have the larger IR-diffraction spot size and larger photon collector

$$D_{SpotSize}(\lambda_{NIR}) = 0.45\mu m, \ d_{CNT}(\lambda_{NIR}) = 0.66nm, \tag{16}$$

as opposed to the smaller yellow diffraction spot size and smaller photon collector at the visible yellow band gap CNT:

$$D_{SpotSize}(\lambda_{yellow}) = 0.051\mu m, \ d_{CNT}(\lambda_{yellow}) = 0.375nm \tag{17}$$

I.3 Two architectures

We compared the relative conversion efficiency of one-layer architecture with that multiple layers, bearing in mind but postponed until the final tradeoff consideration between manufactory difficulty and the cost.

(i)One Basic Layer Architecture:

The architecture contained 16 NIR CNT at 0.66 nm diameter is shown in Figure 2.
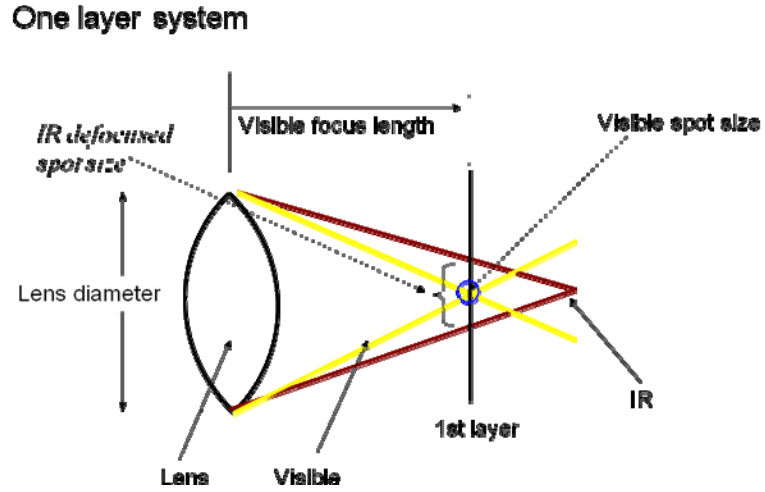

Figure 2. Based on the architecture picture, we computed the total cross section area that the visible yellow light was intercepted by the NIR CNT in a spiral stack of 16 on the visible yellow focal plane.

9

$$A_{CNT\_l} = N_P \cdot d_{CNT}(\lambda) \cdot D_{SpotSize} - a_{overlap\_l} \cdot (N_p - 1)$$

$$= \lambda_{BG}^2 \cdot \left[0.9\gamma_0 \cdot a_{cc} \cdot N_p - \frac{(2\gamma_0 \cdot a_{cc})^2}{1.54}(N_P - 1) \right],$$

$A_{CNTs}(\lambda_{NIR}=1.12 \ \mu m) = 0.00476 \mu m^2,$

$A_{CNTs}(\lambda_{yellow}=0.635 \mu m)=0.0027 \mu m^2$ (18)

where the Rayleigh spot size was focused at yellow light focal plane, which was smaller than that of NIR as indicated on the first layer.

$$A_{SpotSize}(\lambda_{yellow})=0.051 \mu m^2; \ A_{SpotSize}(\lambda_{NIR}) \cong 0.318 \mu m^2 \quad (19)$$

We considered a detail kinetic theory of the charge migration suffering the collision extinction with the neighborhood carrier pairs.

$$N_{phone} \cdot \eta_{Einstein} \cdot (1 - Ex_{collision}) = N_{carrier}$$

$$I_{Total} = qN_{carrier\_NIR} \cdot V_{NIR} + qN_{carrier\_yellow} \cdot V_{yellow}$$

$I_{total\_one\_layer \ at \ Yellow \ FP} / \eta_{Einstein} \cdot (1\text{-}Ex_{collision}) = 9.22 \times 10^3 \text{Amp. in MKS} \quad (20)$
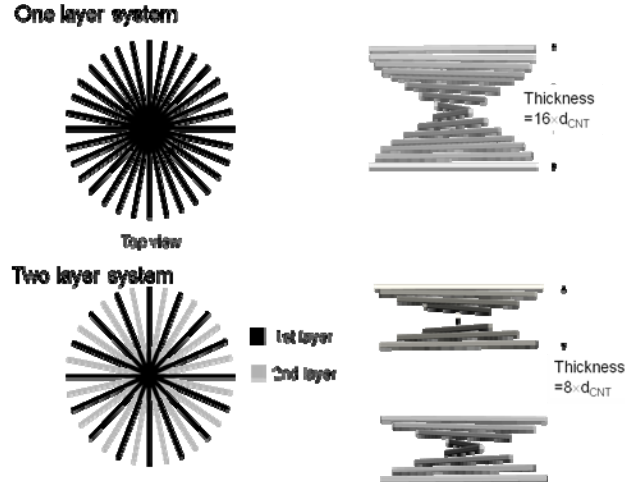
Figure 3. The fan-out pattern of our volume cell is horizontally along the radial direction at every 22° each, the closed packaging of Np=16 NIR CNTs must be overlaid passing one another in the central core creating a stack of tubes like a fireman spiral staircase.

(ii) Two Layers Architecture

We assumed the kinetic velocity of a single charge carrier to be identical at either layers and its velocity depends sole on a single photon energy which has excited the carrier out of the Fermi level after overcome the Einstein surface work potential and transporting along the net field of two asymmetric Schottky barriers at both ends: Palladium (Pd) as P-type and Aluminum Al as N-type.

We focused the yellow light at the focal plane where 8 NIR CNTs were laid in the first layer, then, the rest near infrared (MIR) light was focused at the second layer focal plane where 8 NIR CNTs were laid.

$$\frac{1}{2} m_e \upsilon_{VIS}^2 = \hbar\omega_{VIS} - qW_{Einstein} + q\Phi_{Schottky} \cong \hbar\omega_{VIS}$$

Figure 4. Design model of 3D lens cavity consisting of $8 \times 2 = 16$ CNTs.

As shown in Figure 5, the visible light was focused on the first yellow focal plane laid with

8 NIR CNTs plane

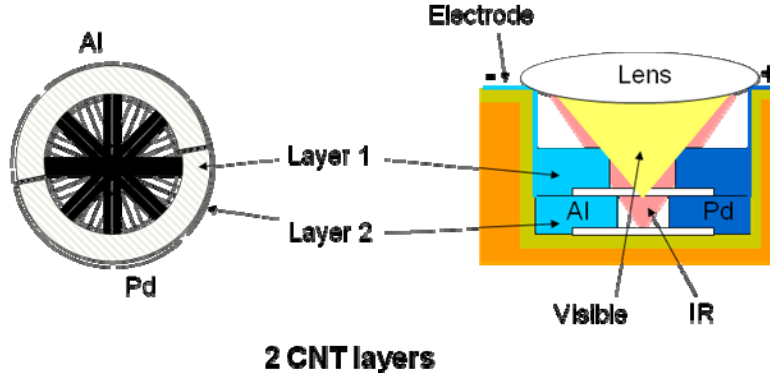$$A_{CNTs} = 0.00134\mu m^2, A_{SpotSize} = 0.051\mu m^2 \tag{21}$$
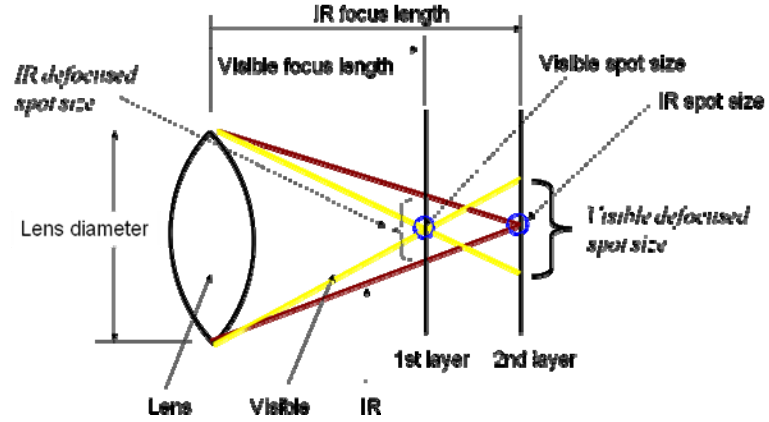
Figure 5   Two Layer Architecture indicated 4 focal spot sizes covered by 8 NIR CNT photon collectors

NIR light was defocused on the first yellow focal plane laid with 8 NIR CNTs plane

$$A_{\text{CNT}} = 0.00334\mu m^2, A_{\text{SpotSize}} = 0.316\mu m^2 \tag{22}$$

Yellow light became defocused on the second NIR focal plane laid with 8 NIR CNTs plane

$$A_{\text{CNT}} = 0.0019\mu m^2, A_{\text{SpotSize}} = 0.102\mu m^2 \tag{23}$$

NIR light was focused on the second NIR focal plane laid with 8 NIR CNTs plane

$$A_{\text{CNT}} = 0.0024\mu m^2, A_{\text{SpotSize}} = 0.158\mu m^2 \tag{24}$$

Then the total energy had two band widths, yellow and NIR, spreading at the first yellow-light-focal plane, produced different numbers of photons:

$$
\begin{aligned}
&Total\_Energy_{yellow}\_at\ 1^{st}\_Layer \\
&= E_{yellow\_1st\_layer}(\lambda_{vis}) \cdot A_{Lens} \cdot \frac{A_{CNT\_yellow}}{A_{SpotSize\_yellow}} = N_{photon\_yellow\_1} \cdot \hbar \cdot \omega_{yellow}
\end{aligned} \tag{25}
$$

$$
\begin{aligned}
&Total\_Energy_{NIR}\_at\ 1^{st}\_layer \\
&= E_{NIR\_1st\_layer}(\lambda_{NIR}) \cdot A_{Lens} \cdot \frac{A_{CNT\_IR}}{A_{SpotSize\_IR}} = N_{photon\_IR\_1} \cdot \hbar \cdot \omega_{NIR}
\end{aligned} \tag{26}
$$

13

The remaining non-intercepted spectrum energy is re-distributed in the second NIR-focal plane

$$Total\_Energy_{yellow}\_2^{nd}\_layer$$
$$= E_{yellow\_2nd\_layer}(\lambda_{yellow}) \cdot A_{Lens} \cdot \frac{A_{CNT\_yellow}}{A_{SpotSize\_yellow}} = N_{photn\_yellow\_2} \cdot \hbar \cdot \omega_{yellow} \qquad (27)$$

$$Total\_Energy_{NIR}\_2^{nd}\_layer$$
$$= E_{IR\_2nd\_layer}(\lambda_{NIR}) \cdot A_{Lens} \cdot \frac{A_{CNT\_NIR}}{A_{SpotSize\_NIR}} = N_{photon\_NIR\_2} \cdot \hbar \cdot \omega_{NIR} \qquad (28)$$

The total number of charge carriers may be estimated in terms of the common efficiency parameter and the transport collision extinction probability.

$$N_{carrier\_yellow} = (N_{photon\_yellow\_1} + N_{photon\_yellow\_2}) \cdot (1 - Ex_{collision})\eta_{Einstein} \qquad (29)$$

$$N_{carrier\_NIR} = (N_{photon\_NIR\_1} + N_{photon\_NIR\_2}) \cdot (1 - Ex_{collision})\eta_{Einstein} \cdot \qquad (30)$$

$$I_{total\_two\_layer} = q \cdot (N_{carrier\_NIR} \cdot V_{NIR} + N_{carrier\_yellow} \cdot V_{yellow})$$

$\Rightarrow N_{photon\_yellow\_1} = 2.7 \times 10^{16}$, $N_{photon\_NIR\_1} = 1.39 \times 10^{16}$,

$\Rightarrow N_{photon\_yellow\_2} = 1.86 \times 10^{16}$, $N_{photon\_NIR\_2} = 1.96 \times 10^{16}$ \qquad (31)

$I_{total\_two\_layer} / \eta_{Einstein} \cdot (1-Ex_{collision}) = 9.42 \times 10^{3}$ AMP in MKS \qquad (32)

I.4 Discussions and conclusions

The physics of Diffraction limit of focus spot size is estimated by Lord Rayleigh about the diameter length $R(z)$, Z_0 is the focus length

$$R(z) = \left(\frac{\lambda \cdot Z_0}{\pi}\right)^{\frac{1}{2}}\left[1+\left(\frac{Z}{Z_0}\right)^2\right]^{\frac{1}{2}} \tag{33}$$

when $Z = Z_0$

$$R_0 = \left(\frac{2\lambda \cdot Z_0}{\pi}\right)^{\frac{1}{2}} \tag{34}$$

It could be expressed to:

$$R = \left.\frac{0.5k\lambda}{NA}\right|_{f_\# < 2} \approx \frac{\lambda}{2} \tag{35}$$

where k is a constant of spot size, NA is numeric aperture ($n \cdot \sin \theta$). F# is of F number $=(Z_0/D)$, D is lens diameter. We can reduce the spot size R by tailoring the refractive index n and increasing the lens diameter, implying a possibility of magnification of the visible solar light within a smaller spot size than that of IR.

Based on the Lord Rayleigh's diffraction-limited focal length known as the Rayleigh range

x (Spot size radius defocus becoming $\sqrt{2}$ factor distance indicated in Figure. 6).

$$x \equiv \frac{\pi \cdot D_{SpotSize}}{\lambda} \tag{36}$$
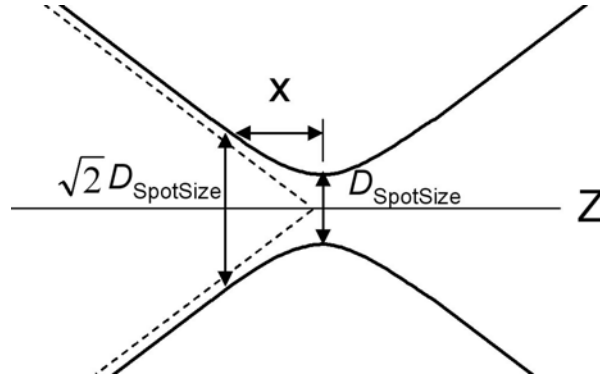
Figure 6. Lord Rayleigh Diffraction Limit Focal Spot

Thus, we can find the wavelength at 0.73 μm, the Rayleigh range x=361 nm, when the wavelength is 1.12μm, the Rayleigh range x= 568 nm. Therefore, the thickness of a stack of spiral NIR CNTs has the total thickness: 16 x 0.66nm=10.56 nm which is about 1% of Rayleigh range. Consequently, the spot size variation of each NIR CNT along the same layer may be neglected.

One layer system puts 16 larger photons collectors made of NIR CNTs onto the yellow light focal plane, compared better than that of two layers having 8 NIR CNTs on each layers.

$$I_{total\_two\_layer}/I_{total\_one\_layer} = 1.02 \tag{37}$$

To increase the efficiency, we exploited the transition regime matter of which the Carbon NanoTube (CNT) is a typical example: the charge carriers along the elongated axial direction follow the classical physics model, while the azimuth cross section of CNT is governed by the quantum physics lattice vibrations, phonons. A higher energy photon which can pass the CNT threshold of higher band gap and producing higher velocity electric current j, along the longitudinal direction which as we said before is valid in classical kinetic theory of current, j=qρv, which is proportional to the charge q, the density ρ, and the velocity v. However, the quantum physics is also valid around the CNT tube cross section, where the de Broglie wavelength of electron wave function is defined as p=h/λ. We must demand the uniqueness of the wave-function when it is going around the circumference of a CNT tube, which is

$$\lambda_{DeBoglie} = \frac{h}{P_{electron}} = n \cdot \pi \cdot d_{CNT}(\lambda_{NIR}) \; ; \; n=1,2, \text{etc.} \tag{38}$$

as Sommerfeld quantization rule has done for Bohr Hydrogen atom, and we have chosen n=1 for the ground state introducing the diameter d of CNT. Thus, we have verified independently Saito band gap formula

$$E_{BG} \approx 1/d_{CNT}. \tag{39}$$

17

This argument demonstrated the nanotechnology of CNT to be valid in the transition regime of both classical and quantum mechanical physics. Thus, we can design from the microscopic semi-conductor Einstein photoelectrical effect to the macroscopically demonstrated Photovoltaic Solar Cell (PVSC) demonstrated in Carbon NanoTube (CNT) first by Li of GE with 2~5% efficiency. We took advantage four more considerations beyond GE experiment: the full spectral, the full polarization, the focusing lens, andthe asymmetric Schottky effect.

The solar cells enjoy seven attributes: (1) the design of multiple spectral layered architecture under the unit optical axis of one simple focusing lens was based on (i) GE, Li APL 2004, demonstrated CNT as PVSE with 5 V dc-bias and 2 symmetric Schottky barriers read-outs, 2%~5% quantum efficiency (QE) for mono or full polarization; (ii) Saito computed the CNT band gap $Eg\sim1/Diameter$. (2) We adopted the Field-Effect Transistor of CNT, without the undesirable dc-bias supply battery in the Space; instead, we employed asymmetric Schottky barriers made of two different metal-semiconductor barriers at both ends of CNT to enhance the Einstein photo-electric e-・-h+ separation to achieve the CCD-like dual read-out. (3) We exploited the Rayleigh diffraction limit focus spot size as a function of the spectral wavelength in Np cross-polarization-bars. (4) over full spectral bands in Ns layers avoiding the shadowing effect to enhance the total QE without the wasteful fill factor. (5) 1-D CNT enjoys less thermal noise in wasted heat $\sim1/2 KBT=1/40$ eV. (6) ~O(N) PIN-OUT dual CCD-like Circuitry. (7) We minimize the kinetic recombination of neighborhood electrons and holes in the phase space of the full

2D surface with spiraling charge carriers. Our analysis of the optics throughput efficiency indicated the trade-off design of a circuit of 2 different metal-semi-conductor Schottky Barrier contact electrodes for 16 CNT = Ns(2) · Np(8) sources, rather than original proposal of 16 CNT=4×4 in the 3D cavity structure which tracks the bare sun automatically in the Space and absorbs the dominated solar spectrum energy and thus can increase the total quantum efficiency.

I.5 References

1. J.U. Lee, "Photovoltaic effect in ideal carbon nanotube diodes," Appl. Phys. Lett., 87, 073101 (2004)

2. H. Ou and H. Szu, "Designs of solar voltaic cells based on carbon nano-tubes" Proc. SPIE, 6247, 62470F, (2006)

3. S. Srivastava, N.K. Swami, and G.P. Srivastava, "Efficiency of Schottky Barrier Solar Cells," Phys. Stat. Sol. 58, 343 (1980)

4. M.H. Yang, K.B.K. Teo, W.I. Milne, and D.G. Hasko, "Carbon nanotube Schottky diode and directionally dependent field-effect transistor using asymmetrical contacts," Appl. Phys. Lett., 87, 253116 (2005).

5. P. Bai, E. Li, K.T. Lam, O. Kurniawan and W.S. Koh, "Carbon nanotube Schottky diode: an atomic perspective," Nanotechnology 19. 115203 (2008).

6. Courtesy V. Klimov, Los Alamos National Laboratory

7. W. Shockley and H.J. Queisser, "Detailed Balance Limit of Efficiency of p-n Junction Solar Cells," J. Appl. Phys. 32, 510-519 (1961).

8. Department of Energy on the web at http://www.sc.doe.gov/reports/files/SEU_rpt.pdf.

9. R. Saito, G. Dresselhause, M.S. Dresselhaus, "Physical Properties of Carbon Nanotubes," Imperial College, London, (1998).

10. H. Urey, "Spot size, depth-of-focus, and diffraction ring intensity formulas for truncated Gaussian beams," Appl. Opt. 43, 620 (2004).

11. J.W. G. Wildoer, L.C. Venema, A.G. Rinzler, R.E. Smalley and C. Dekker, "Electronic structure of atomically resolved carbon nanotubes," Nature 391, 59-62 (1998).

12. J. Guo, C. Yang, Z.M. Li, M. Bai, H.J. Liu, G.D. Li, E.G. Wang, C.T. Chan, Z. K. Tang, W.K. Ge, and X. Xiao, "Efficient Visible Photoluminescence from Carbon Nanotubes in Zeolite Templates," Phys. Rev. Lett. 93, 017402-1 (2004).

13. D.A. Stewart, and F. Lonard, "Energy Conversion Effiiciency in Nanotube Optoelectronics," Nano Lett., 5, 219-222 (2005).

14. B. Kannan, K. Castelino, and A. Majumdar, "Design of Nanostructured Heterojunction Polymer Photovoltaic Devices," Nano Letters, 3 (12), 1729 -1733, 2003.

15. N.K. Swami, S. Srivastava, and H. M. Ghule, "The role of the interfacial layer in Schottky barrier solar cells," J. Phys. D : Appl. Phys., 12, 765 (1979)

II. Summary of work in nanoindentation of elstoplastic and viscoelastic materials

II.1 Nanoindentation in an Elastoplastic Material

Nanoindentation is an experimental method used to characterize materials at the nano and micro scale. During a nanoindentation test a diamond indenter tip is pressed into a material up to a specified force or depth and then withdrawn. As the test is performed, the indentation force and depth are recorded and results are normally presented in the form of a load-displacement curve. This load-displacement curve may be used to determine different material properties and characteristics (Oliver, 2004; Mencik, 2007). An important factor in examining the results is the type of tip used in indentation. Berkovich indenters are one of the most common types of indenter tips used. A Berkovich tip is faceted in the form of a three sided pyramid. Information relating to stress-strain behavior in an elastoplastic material during loading and unloading may be provided by finite element analysis. The commonly used Berkovich indenter with its three sided pyramidal geometry must be modeled and analyzed as a 3D contact problem in finite element simulations. However, the common approach in finite element simulation is to use a 2D axisymmetric indentation model which uses a conical shaped indenter as an equivalent to a Berkovich indenter (Knapp, 1999; Panich, 2004; Pelletier, 2000). The main reason for this approximation is that the 3D contact problem may require a large amount of computational resources and usually takes a long time to complete, especially when using a fine 3D mesh for accurate results. To overcome these challenges, a 70.3° half-angle conical indenter is often used as a substitute for modeling the Berkovich tip, on the bases that it provides the same indentation

depth to projected area ratio of a Berkovich indenter. By using a conical indenter the finite element analysis can be simplified by using a 2D axisymmetric model which allows for quicker simulations using fewer computer resources. Since this is a common approach for the finite element analysis of indentation problems it is important to compare the finite element analysis results for both conical and Berkovich indentations to investigate any deviations in behavior between the two. While there have been several recent studies comparing finite element simulations for the two indenters, the results presented by different investigators are not in full agreement.

The objective of this thesis is to present a detailed finite element study of nanoindentation in order to gain additional insights into the effect of tip geometry on the force-displacement curves obtained in nanoindentation tests. The previous studies used different elastoplastic models including the use of different power-law hardening and the use of elastic-perfect plasticity. This study will investigate the behavior of conical and Berkovich indenters for materials obeying a combined isotropic and kinematic hardening.

II.1.2 Literature Review

One of the earliest studies that numerically compared different indenter tips was performed by Li et al. (2004). In their study they compared several types of indenters, Berkovich, Vickers, and Knoop to several different conical indenters with half angles that were determined by different equivalency rules. The study provides simulations with indentation depth of approximately 1000nm in an elastoplastic material with isotropic hardening. The load-displacement curves by Li et al. (2004) show close agreement between

the Berkovich result and the conical result with the Berkovich load being slightly higher in the mid range of indentation depth. The authors conclude that stress fields between Berkovich and conical indenters are different and if stress field is of interest a 3D simulation is called for. However, if only load-displacement curve is needed then the Berkovich indenter can be sufficiently simulated by a conical indenter (Li, 2004).

Swaddiwudhipong et al. (2006) also attempt to address equivalency of Berkovich and conical indenters by performing 2D and 3D finite element analysis to simulate the load-displacement response in elastoplastic materials. Indentation simulations were performed for both conical and Berkovich indenters using different materials, including 6061 aluminum, that are set to obey power-law strain hardening. Indentations were simulated to a relatively deep 5μm. The paper provides a load-displacement curve comparing conical and Berkovich indentations in 6061 aluminum. In this curve the Berkovich indentation curve is noticeably lower than that of the conical indentation. The authors conclude that the equivalency between the two types of indenters in terms of the curvature of the load-displacement curve is not valid across the range of material properties considered (Swaddiwudhipong, 2006).

Finite element simulations of nanoindentation in elastoplastic materials with no hardening were performed by Xu and Li (2008) to study the effects of indenter geometry and mechanical properties of the indented material. The indenter geometries considered were conical and Berkovich. The study was specifically looking at correction factor but there are also plots that directly compare load-displacement behavior of both indenter

types. In the provided plots the Berkovich indentation curves are noticeably higher than those for the conical indenter across the range of material properties shown in the paper. The difference is explained as a geometry effect with the difference being more noticeable for harder materials (Xu, 2008).

Another investigation into the effect of indenter geometry on indentation test results was performed by Sakharova et al. (2009). Conical and Berkovich were among the indenter geometries examined. Elastoplastic indentations using Swift hardening law (Wang, 2005) were simulated using an in-house finite element code. The load-displacement plots provided in the paper show that the responses from the different indenters were very similar. Small differences in the curves were observed when the ratio of the residual indentation depth after reloading and the indentation depth at maximum load (hf/hmax) was below 0.65. In these cases the Berkovich indenter curves were slightly higher (Sakharova, 2009).

Comparisons between the load-displacement responses of materials indented by conical and Berkovich indenters using finite element analysis have been presented in these earlier studies. However, the results do not seem to show a consistent trend and therefore investigation into the equivalence between these two types of indenters is still incomplete.

II.1.3 Material Modeling

II.1.3.1 Description of the Constitutive Model

The combined isotropic/kinematic hardening model is a pressure-independent J2 plasticity model that can be used for modeling materials. The behavior of the material is dependent on an elastic component and a plastic component. To show this the strain rate can be written in terms of a plastic and elastic component

$$\dot{\boldsymbol{\varepsilon}} = \dot{\boldsymbol{\varepsilon}}^{el} + \dot{\boldsymbol{\varepsilon}}^{pl} \tag{1.1}$$

The elastic component is isotropic and linear. It is dependent of two material parameters bulk modulus, K, and shear modulus, G. The parameters are calculated based on the Young's modulus, E, and Poisson's ratio, v

$$K = \frac{E}{3(1-2v)} \tag{1.2}$$

$$G = \frac{E}{2(1+v)} \tag{1.3}$$

Using these parameters elasticity can be decomposed into volumetric and deviatoric components

$$p = -K\varepsilon_p \tag{1.4}$$

$$q = 3G\varepsilon_q \tag{1.5}$$

For plastic behavior the isotropic/kinematic model is used with the Mises yield surface in ABAQUS (Simulia, 2010). The yield surface is given by the function

$$f = \frac{3}{2}(\mathbf{S} - \boldsymbol{\alpha})(\mathbf{S} - \boldsymbol{\alpha}) - k^2 \tag{1.6}$$
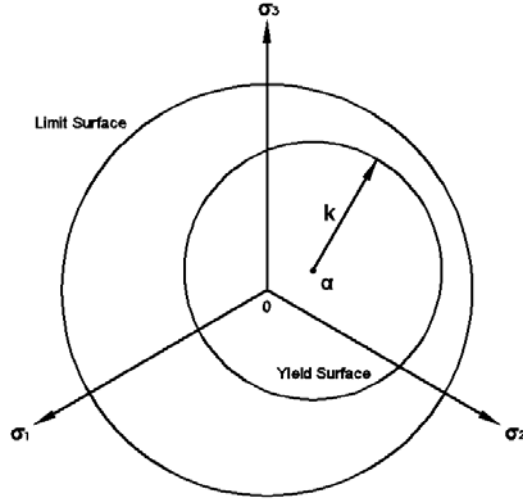
25

Figure II.1-1: Yield surface of combined isotropic/kinematic hardening model.

In the yield surface equation $\mathbf{S}$ is the deviatoric stress tensor which is defined as $\mathbf{S} = \boldsymbol{\sigma} + p\mathbf{I}$, $\boldsymbol{\alpha}$ is the deviatoric component of the backstress tensor, and k is the size of the yield surface. The backstress creates a translation of the yield surface in the stress space. This shift can be seen in the preceding figure of the yield surface. A Mises yield surface without kinematic hardening would remain centered along the hydrostatic axis. With the kinematic hardening the backstress translates the yield surface so that the center is no longer coincident with the hydrostatic axis.

Associated plastic flow is assumed for the model which gives

$$\dot{\boldsymbol{\varepsilon}}^{pl} = \dot{\overline{\varepsilon}}^{pl} \frac{\partial f(\boldsymbol{\sigma} - \boldsymbol{\alpha})}{\partial \boldsymbol{\sigma}} \tag{1.7}$$

$$\dot{\overline{\varepsilon}}^{pl} = \sqrt{\frac{2}{3}\dot{\boldsymbol{\varepsilon}}^{pl} : \dot{\boldsymbol{\varepsilon}}^{pl}} \tag{1.8}$$

26

Where $\dot{\bar{\varepsilon}}^{pl}$ is the equivalent plastic strain rate and $\dot{\boldsymbol{\varepsilon}}^{pl}$ is the rate of plastic flow.

Hardening consists of a kinematic component and an isotropic component. The components of the kinematic hardening are the backstresses, of which there can be several. The hardening law for each backstress is given as

$$\dot{\boldsymbol{\alpha}}_k = C_k \frac{1}{\sqrt{k}} (\boldsymbol{\sigma} - \boldsymbol{\alpha}) \dot{\bar{\varepsilon}}^{pl} - \gamma_k \boldsymbol{\alpha}_k \dot{\bar{\varepsilon}}^{pl} \tag{1.9}$$

$$\boldsymbol{\alpha} = \sum_{k=1}^{N} \boldsymbol{\alpha}_k \tag{1.10}$$

The total number of backstresses is N, and C_k and γ_k are material parameters that are calibrated in ABAQUS based on test data. The values C_k are the initial kinematic hardening moduli, and γ_k determine the rate of decrease of the kinematic hardening moduli corresponding to an increase in plastic deformation (Simulia, 2010).

The evolution of the size of the yield surface, k, is defined by the isotropic hardening behavior of the model. The yield surface size evolution is a function of the equivalent plastic strain, $\bar{\varepsilon}^{pl}$, and can be written as

$$k = \sigma |_0 + Q_\infty (1 - e^{-b\bar{\varepsilon}^{pl}}) \tag{1.11}$$

Where $\sigma |_0$ is the size of the yield surface when plastic strain is zero. The maximum change in the size of the yield surface is given by Q_∞, and b affects the rate of change of the yield surface size while plastic strain develops. The parameters Q_∞ and b are obtained through calibration with test data (Simulia, 2010). In the kinematic hardening model, the kinematic hardening component causes a shift of the center of the yield surface in stress

27

space. The isotropic component can expand or contract the yield surface range. These components allow for the modeling of elastoplastic behavior of materials.

II.1.3.2 Calibration of Material Model

The experimental results and numerical simulations presented in this paper were performed on 6061 aluminum as a typical elastic–strain hardening plastic material. To evaluate the mechanical properties of this material, a macro scale uniaxial test was conducted and the observed stress–strain curve was used to calibrate the constitutive model used in the finite element analysis. All analyses were conducted using ABAQUS (Simulia, 2010). In ABAQUS a metal plasticity constitutive model with combined isotropic/kinematic hardening was used to model the aluminum. Calibration of the combined isotropic/kinematic hardening model in ABAQUS requires half-cycle stress–strain test data. To acquire the required data a uniaxial tension test was performed on a "dog bone" specimen of 6061 aluminum. During the test the sample was loaded in uniaxial tension, once it reached initial yield stress the sample was unloaded and reloaded to yield again. The unloading and reloading process was repeated for two additional cycles. Stress and strain data were recorded throughout the test.

Table II.1-1: Evolution of yield stress with plastic strain.

Plastic strain	0.0	0.002	0.01605	0.04667	0.07511
Yield stress (kPa)	300,000	307,500	317,181	325,620	330,831

From the initial elastic loading data the Young's modulus (E) was calculated as approximately 65GPa. A Poisson's ratio (ν) of 0.33 was assumed. Given the value of Young's modulus, the strain hardening data relating the yield stress to plastic strain were obtained from the test results. Table II.1-1 shows the tabulated values of yield stress versus plastic strain. This data was used to calibrate the elastoplastic constitutive model.

The calibration process was performed by conducting a plane stress simulation of a single finite element subjected to displacements that approximate those applied in the uniaxial tension test. After conducting a series of simulations and adjusting the number of back stresses to five for smoothing the elastoplastic transition, the finite element model provided a good simulation of the 6061 aluminum stress–strain behavior, as shown in Figure II.1-2.
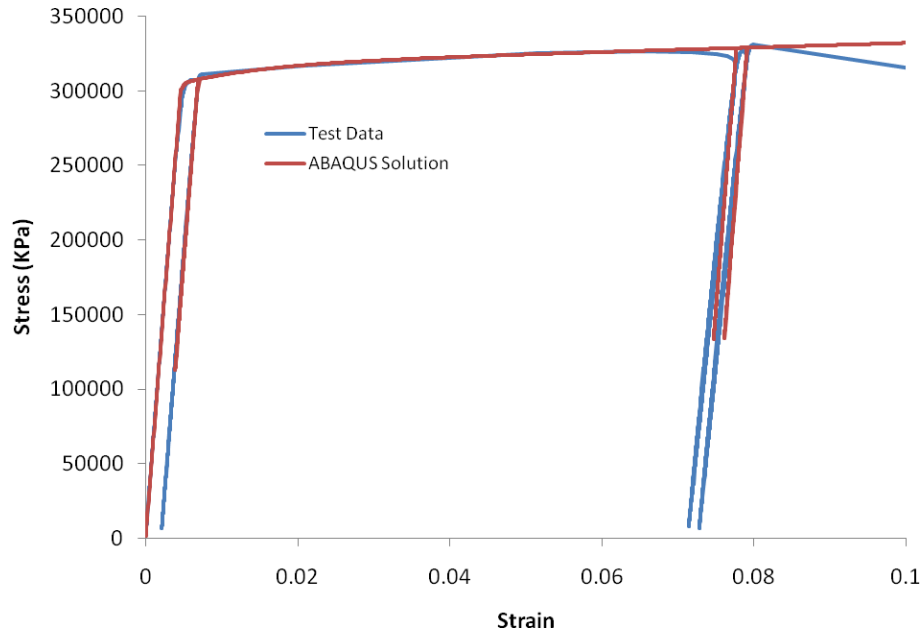
Figure II.1-2: Comparison of experimentally obtained stress–strain curves with the simulation of a combined isotropic/kinematic hardening plasticity model for 6061 aluminum.

II.1.4 Finite Element Modeling

In this study three different finite element nanoindentation models were investigated using the commercial finite element analysis program ABAQUS. The first model was a 2D axisymmetric model using a conical indenter. This type of model is commonly used in research and allows for relatively quick computation. The second model was a 3D finite element model with a conical indenter tip. This model, which is the full 3D equivalent to the 2D model, was used to confirm the suitability of the 3D finite element mesh. The third model was a 3D finite element mesh that included complete geometric representation of Berkovich tip. This model allows for a thorough comparison of Berkovich tip to the

30

assumed equivalent conic tip advocated in literature. Tip geometries for all the above

models include a 200nm tip radius to simulate a used indenter tip.

II.1.4.1 Verification of the 2D Finite Element Model

The first step was to create and verify a 2D axisymmetric nanoindentation model in

ABAQUS. The performance of the developed model was verified against the available

results in literature. As part of his Ph.D. thesis, Poon (2009) performed a series of finite

element simulations of elastic indentations while adjusting the radius and height of the

specimen. These simulations suggest the proper specimen size to approximate a body of

semi-infinite extent for a given indentation depth. Reproducing the key results of Poon's

simulation helped verify the quality of the finite element mesh and the sizing of the

material dimensions used in the present study.

Poon (2009) initially provided a simulation for an axisymmetric indentation onto the

top surface of a cylindrical specimen with a radius, r_s, of 18μm and a height, h_s, of 30μm.

The specimen was modeled as an elastic isotropic deformable solid with E=70GPa and

ν=0.3. The 70.3° half-angle "Berkovich equivalent" conical indenter was modeled as an

analytical rigid surface with a tip radius of ρ=200nm. The maximum indentation depth was

h_{max}=600nm. The finite element mesh was described as using 5006 three-node linear

axisymmetric triangular elements (CAX3) with a higher mesh density at the indentation

site. For later simulations the number of nodes was scaled depending on the specimen

dimensions. Contact between the indenter and specimen was modeled as frictionless.
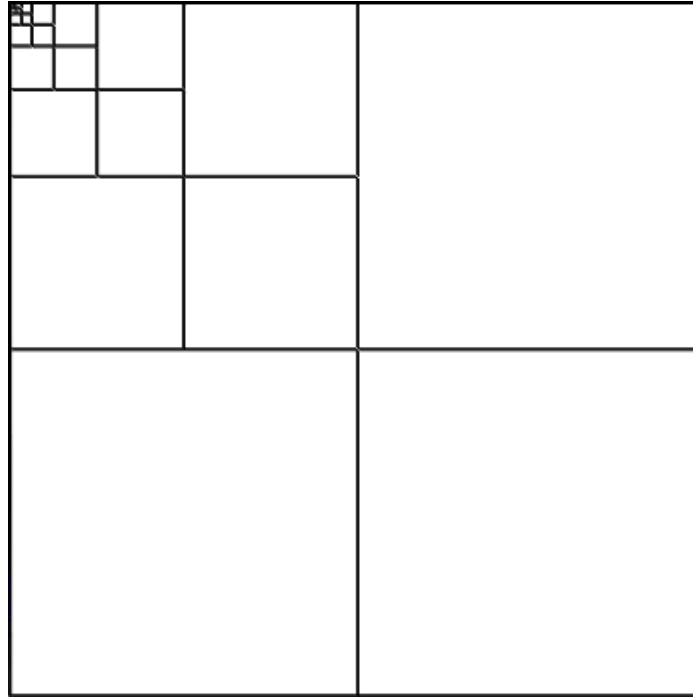
Figure II.1-3: Face partitioning of 2D axisymmetric specimen.

A 2D axisymmetric model was created for the present study using the same parameters detailed in Poon (2009). While CAX3 element type was used, a different finite element mesh was constructed to see the potential effects of mesh configuration. The specimen was modeled with editable dimension constraints for the radius and height. The face of the specimen was then partitioned into quarters. In order to easily provide a higher density mesh at the indentation site the quadrant containing the indentation site (upper left) was quartered. This last step was repeated until the face in the corner of the indentation site was sufficiently small. The resulting face partition of the specimen is shown in Figure II.1-3.

Edges were then seeded to provide a high mesh density at the indentation site and less density further away as shown in Figure II.1-4.
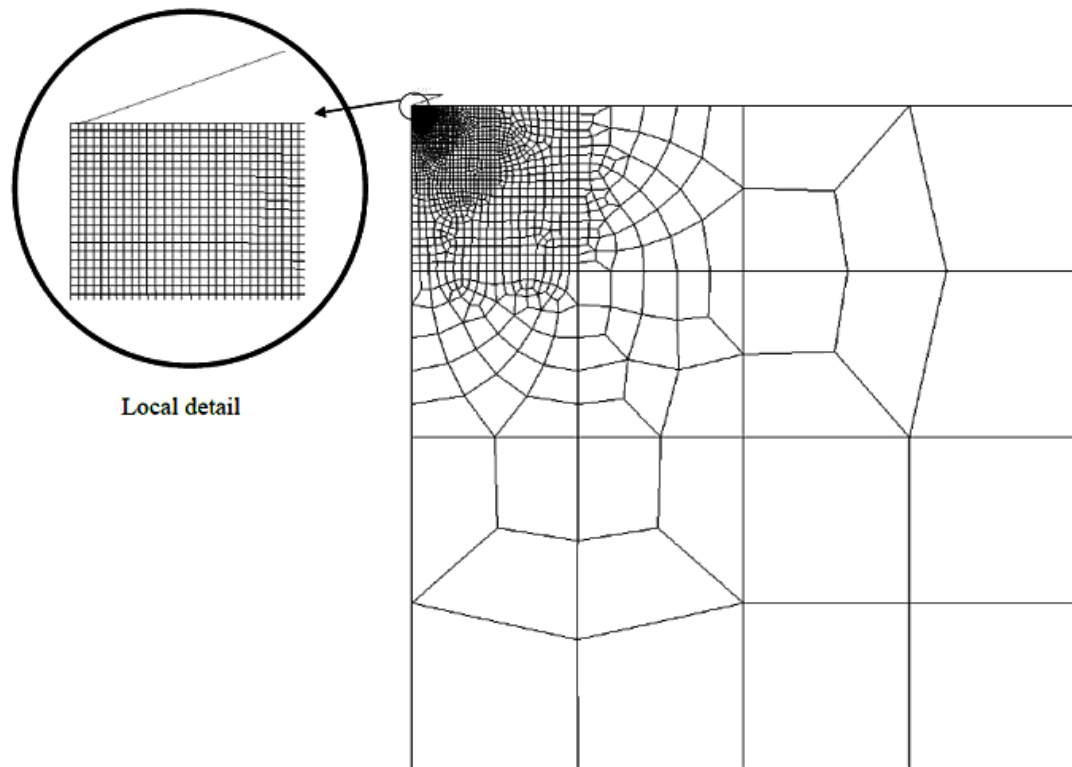

Local detail

Figure II.1-4: 2D axisymmetric finite element mesh of the specimen.

A linear elastic analysis was performed using the same material size and specifications used in the initial Poon simulation. Figure II.1-5 shows the load-displacement result obtained from this simulation and compares it to the simulation result presented in Poon (2009). The curves were in good agreement with only slight differences which may be caused by errors in reading the values from the curves in Poon (2009).
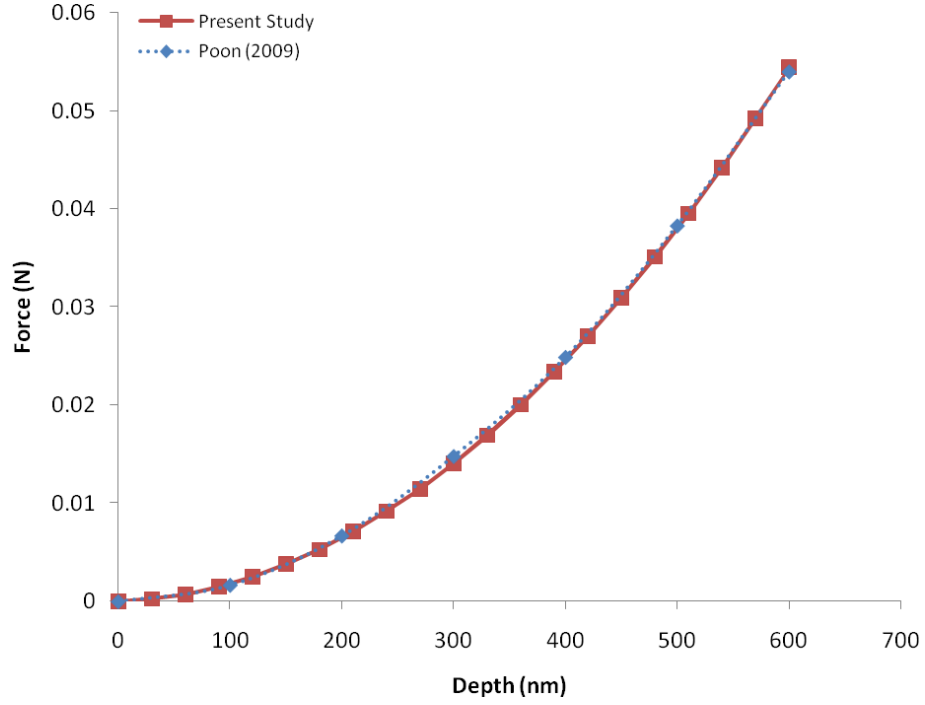
Figure II.1-5: Load-displacement comparison for elastic indentation simulation into a specimen with r_s=18μm and h_s= 30μm.

More verification simulations were conducted by varying the tip radius of the indenter. The specimen in these simulations was described as having converged geometry. Converged geometry is determined by using the following relations:

$$\frac{r_s}{h_s} \geq 1 \qquad (1.12)$$

$$\frac{h_s}{h_{max}} \geq 100 \qquad (1.13)$$

The result is shown for the range of indentation of approximately 260nm, though the actual indentation depth is not given. To reproduce the results for this study an indentation depth of 300nm was used on a material with r_s= 30μm and h_s= 30μm. Load-displacement results are shown in Figure II.1-6. The results show good agreement in values and trends when compared with those obtained by Poon (2009).
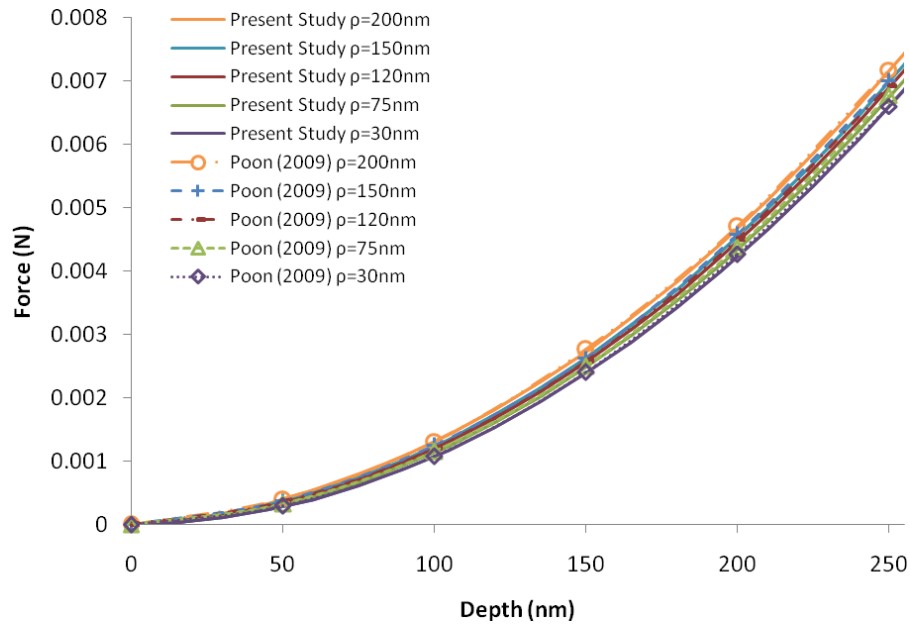

Figure II.1-6: Load–displacement comparison for elastic indentation simulation into a specimen with varying indenter tip radii, ρ (30, 75, 120, 150 and 200 nm).

Simulations were also performed keeping the same specimen radius of r_s=18μm, while varying the specimen height, h_s, through the values 18, 30, 40, 60, 92, and 120μm. The load-displacement results for the simulations are shown in Figure II.1-7. The results exhibit the expected trend where load increases with decreased specimen height.

For further simulations in the study the material dimensions are chosen to be r_s= 60μm and

h_s= 60μm to accommodate indentations of up to 600nm according the convergence

relations provided.
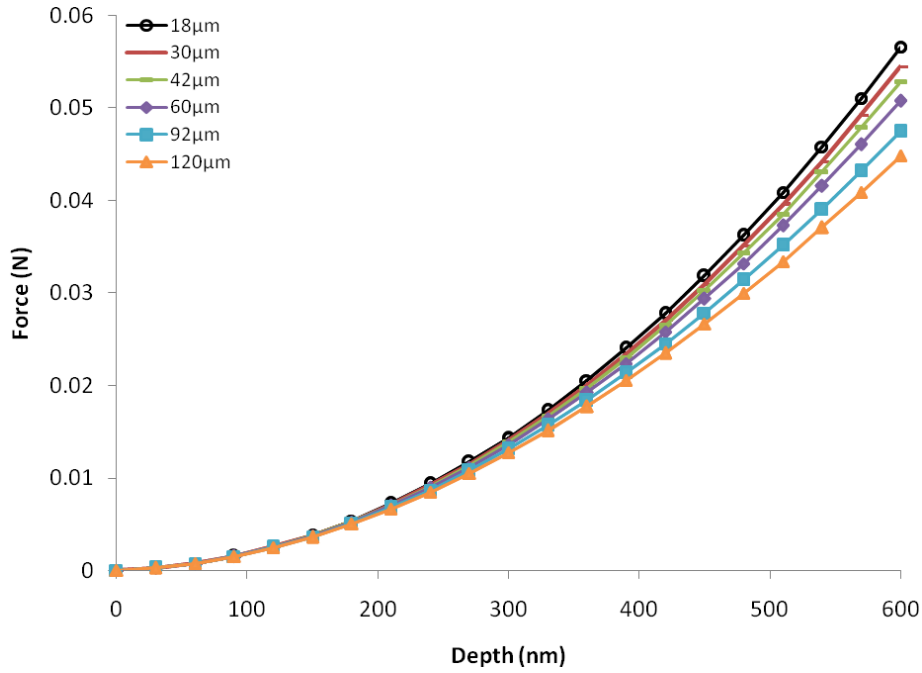
Figure II.1-7: Load–displacement curves for elastic indentation simulation into a specimen with rs = 18 μm and varying hs (18, 30, 42, 60, 92 and 120 μm).

II.1.4.2 Two and Three Dimensional Elastoplastic Simulations

The 2D axisymmetric finite element mesh was verified for elastic indentation. To

perform elastoplastic indentations the calibrated elastoplastic constitutive model was used.

The material specimen was sized to accommodate indentations up to a 600nm. The element

type in the mesh was changed to a four-node bilinear axisymmetric quadrilateral element

(CAX4R), which for linear elastic analysis would produce the same results as those obtained by the CAX3 element used in verification studies discussed earlier.

Initial elastoplastic simulations resulted in load-displacement curves that exhibited a slight oscillation or "stepping type" behavior in the load-displacement curve. This behavior was corrected by providing a more uniform grid for the fine mesh around the indentation site. The mesh was verified through a convergence study of the 2D elastoplastic indentation as shown in Figure II.1-8. The final mesh chosen included 8,582 elements. The 2D analysis results were later used as a baseline for comparison against the 3D indentation models. Figure II.1-4 shows the 2D axisymmetric mesh with a detail of the local mesh near the indenter tip.
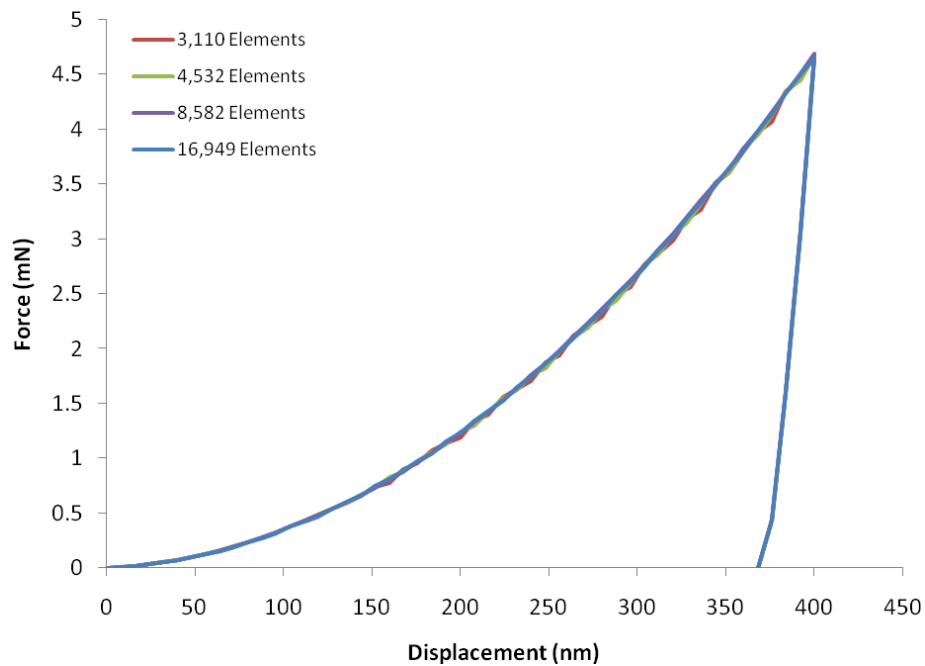

Figure II.1-8: Comparison of the simulations using different 2D axisymmetric finite element meshes in elastoplastic indentation for 6061 aluminum.

37

To provide confirmation of the suitability of 3D meshes and for direct comparison to the 2D model, a 3D conical tip nanoindentation model was first created. Similar to the 2D model the 3D indentation model was created using a 70.3° half-angle Berkovich equivalent cone. The conical indenter was created as a revolved shell analytical rigid surface as shown in Figure II.1-9.

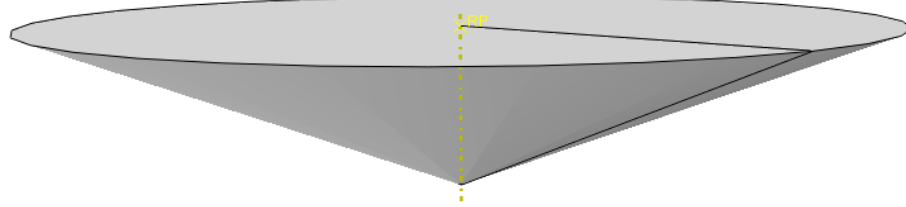Figure II.1-9: 3D model of 70.3° half-angle conical indenter.

The specimen was created in a cylindrical shape with the same depth and radius as the 2D axisymmetric model and elastoplastic material parameters were also identical to those used in the 2D axisymmetric model. The finite element mesh of the specimen was created so that it was fine on the surface around the site of indentation as well as the initial depth of the cylinder. The mesh was then increasingly coarsened in the areas that were further away from the indentation site. Each quadrant of the specimen's top surface was meshed by using a method similar to that used in the 2D axisymmetric model, i.e., creating increasingly smaller square partitions and then seeding the edges for desired mesh density. The element type was chosen to be an 8-node linear brick using reduced integration and

38

hourglass control (C3D8R). Figure II.1-10 shows the 3D finite element mesh and a local mesh detail near the tip is shown in Figure II.1-11.
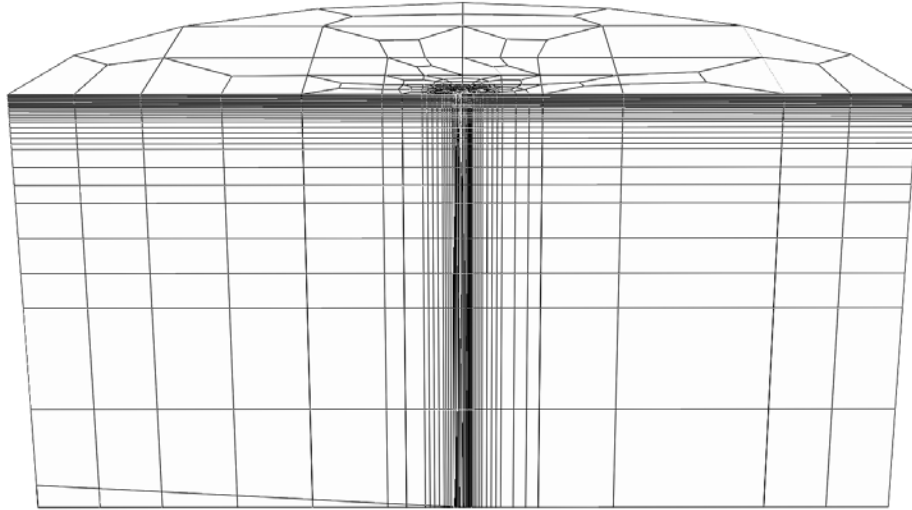

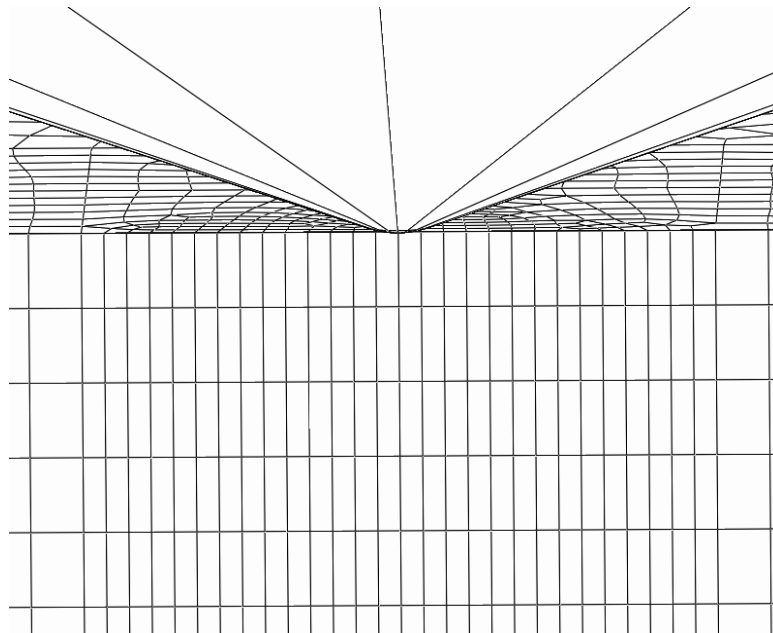Figure II.1-10: 3D finite element mesh of the specimen.

Figure II.1-11: Local details of 3D finite element mesh near the indenter.

A 3D Berkovich tip nanoindentation model was the third and final finite element mesh created for analysis and comparison. The material model and the finite element mesh of the specimen were carried over from the conical simulation. The main difference between the two 3D models was the tip geometry. The Berkovich tip was modeled as a three sided pyramid with a semi-angle between vertical and each face of 65.27°. An area of difficulty in modeling the Berkovich tip was in the process of rounding the tip. A pyramidal shape cannot be tangentially rounded by a sphere along all sides and edges. Instead the tip was rounded using the intersection between a sharp Berkovich geometry and a conical geometry with a 200nm tip radius and a half angle of 77.05° which is equivalent to the semi-angle to the sharp edges of a Berkovich pyramid. Due to the complexity in the Berkovich tip geometry it cannot be treated as an analytical rigid surface, instead it was modeled as a discrete rigid surface. A 3D model of the Berkovich indenter tip is shown in Figure II.1-12.
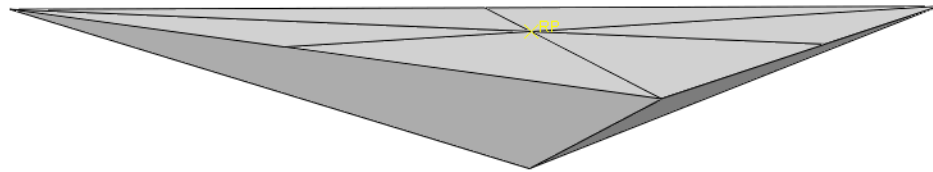
Figure II.1-12: 3D model of Berkovich indenter.

After some preliminary simulations, slight adjustments were made to the specimen mesh for the Berkovich indentation to accommodate interaction with the more complicated

40

Berkovich tip geometry. Distortions in the mesh would arise depending on the orientation of elements that were contacted by the pyramid edge. The mesh was modified in the region of tip contact to align element edges with the pyramid edges. This correction reduced mesh distortion and provided an improvement in the load-displacement response. A local detail of the improved mesh configuration is shown in Figure II.1-13.

Figure II.1-13: Local top surface details of the modified 3D finite element mesh configured to improve interaction with Berkovich indenter.

All three finite element models shared several common characteristics. The elastoplastic material properties used were those obtained from the uniaxial tension test of

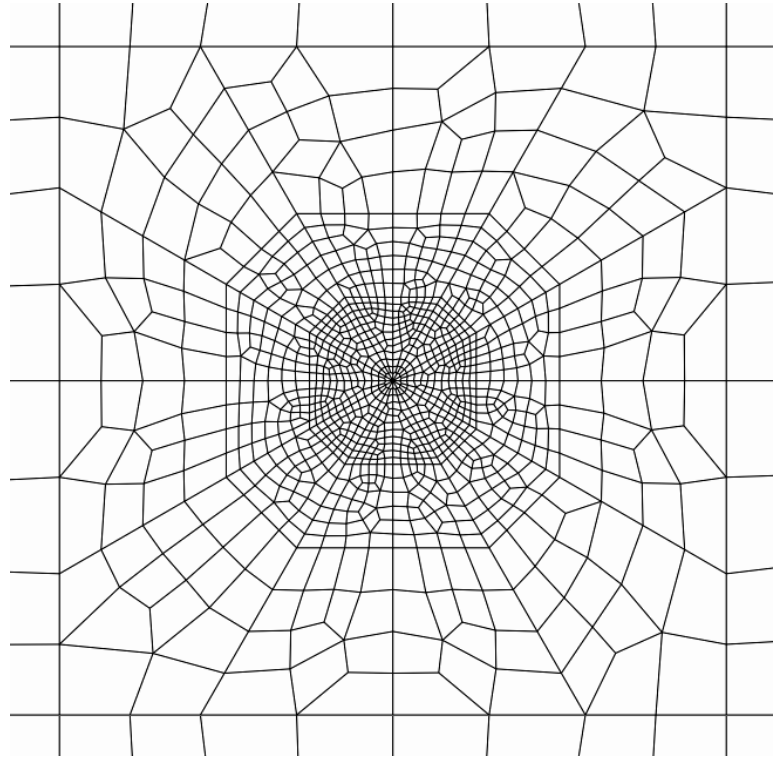6061 aluminum. Contact was modeled as frictionless between the indenter and material. Displacement of the indenter was applied through a displacement boundary condition applied to a reference node of the rigid indenter surface. Indentation force was obtained by requesting output of the reaction force at the reference node during the analysis.

Results in the study were all obtained from ABAQUS implicit analysis. However, explicit analysis was also considered. Simulation results revealed that explicit analysis would work well for analysis of a 3D cone since it provided a response very similar to that of the implicit analysis. However, the explicit analysis provided poor results for the Berkovich indentation. The poor performance was attributed to large elemental distortion of the material in regions of the mesh that had contact interaction with the edges of the Berkovich pyramid. This led to a decrease in simulation accuracy with increased mesh refinement due to larger relative distortions for the finer elements. These large distortions not only led to inaccuracy but the unexpected behavior where the material would pull back on the indenter resulting in a negative reaction force during unloading. Figure II.1-14 shows an example of the mesh distortion experienced in an explicit analysis. Implicit analysis was confirmed to be the preferable method for nanoindentation simulation.
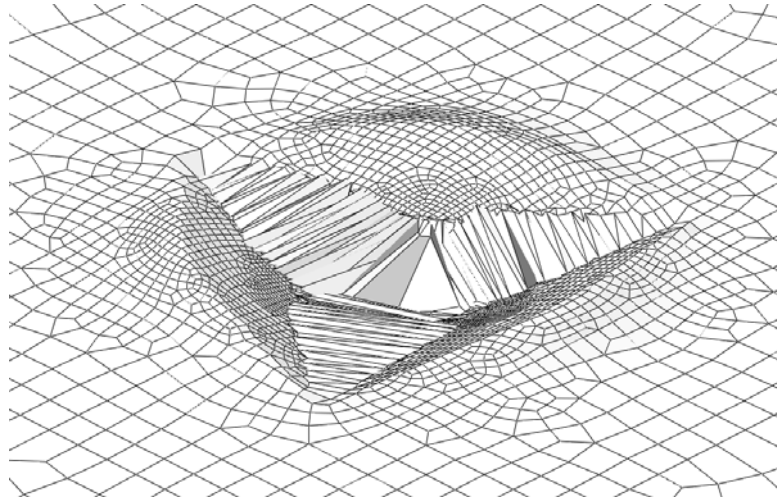
Figure II.1-14: Mesh distortion observed in explicit simulation of Berkovich indentation.

Using these three finite element models, a comparison of how geometry affects the indentation results can be made. The main point of interest was how similar the load-displacement behavior was between a Berkovich indenter and the equivalent conical indenter.

43

II.1.5 Results and Discussion

II.1.5.1 Finite Element Simulations of Nanoindentation

The results were first examined by considering the load-displacement curves of the elastoplastic indentation process. The load-displacement curve represents the overall material reaction to the nanoindentation process and it also represents what would be recorded during a nanoindentation experiment. An indentation depth of 400nm was chosen in this comparison study.

Figure II.1-15 compares the load-displacement results obtained from a 2D axisymmetric conical indentation simulation and a 3D conical indentation simulation. It would be expected that both simulations would provide the same curve. In line with expectations the two curves are in good agreement with each other. At maximum indentation depth the difference between the two curves is less than 2%. The differences may be attributed to the fact that the mesh of the 2D axisymmetric model is much finer than the 3D conical model in the area around the tip. Increasing the mesh refinement in the 3D model would lead to significant increases in simulation time while producing little improvement in the simulation results. Hence, the 3D finite element mesh was considered to be sufficiently refined.

Figure II.1-16 shows a comparison of the load-displacement curves for the Berkovich and conical indenters. It can be seen that there is a difference between the results. The Berkovich indentation curve is noticeably lower than that of the conical indenter. According to common practice the curves should match if the projected area to indentation

depth is equal. The contact area during indentation was then checked for both indenter geometries to determine if there are differences in contact area that are leading to load differences. Figure II.1-17 shows the contact area for both Berkovich and conical indenters as it relates to indentation depth in the simulations. The contact area curves for the two indenters have slight differences but in general they are very similar to each other.
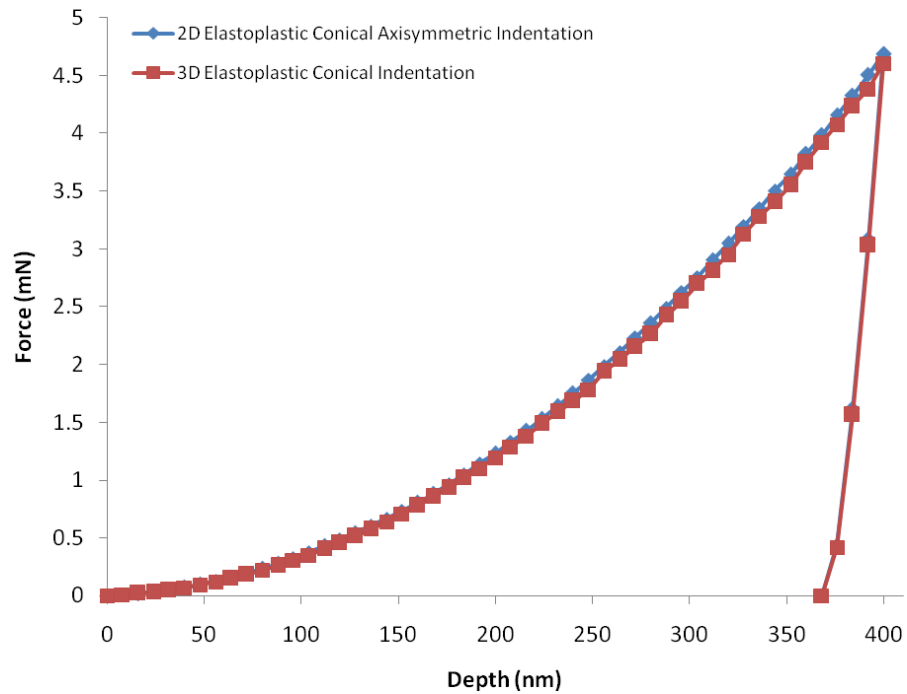

Figure II.1-15: Comparison of load–displacement curves for 2D and 3D conical indentation simulations in 6061 aluminum.
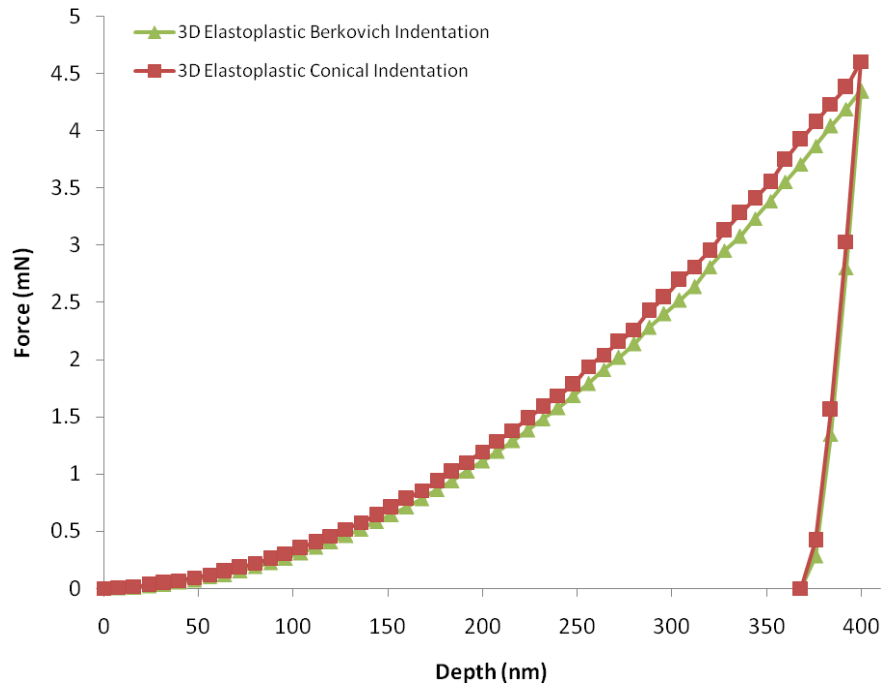
Figure II.1-16: Comparison of load–displacement curves for conical and Berkovich indentation simulations in 6061 aluminum.
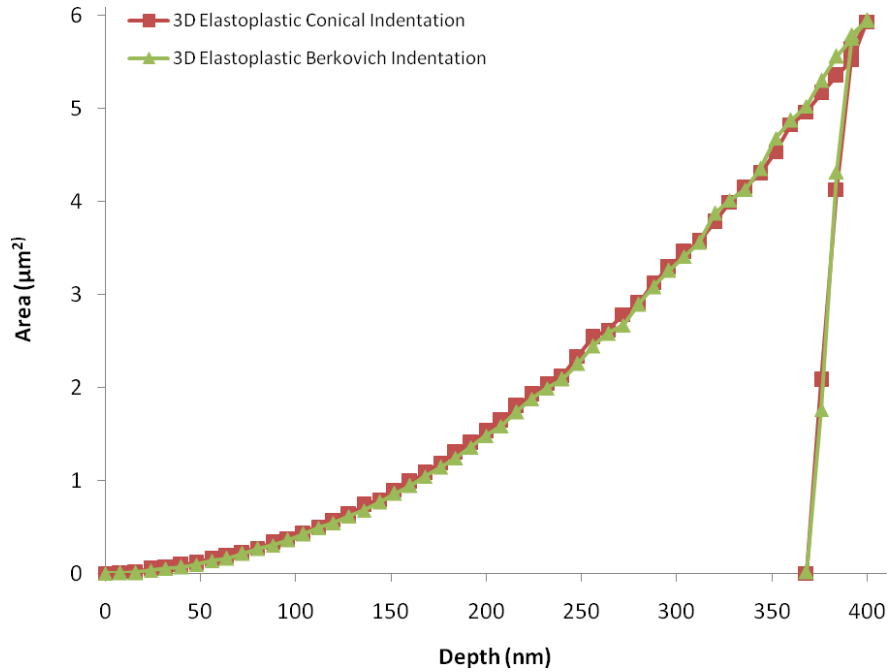
Figure II.1-17: Comparison of contact areas computed in conical and Berkovich indentation simulations in 6061 aluminum.

The contact areas for Berkovich and conical indenters are essentially the same but there load-displacement curves have noticeable differences; this provides good motivation to examine the normalized contact stresses for the two indenters. The normalized contact stresses during indentation for the two indenters is shown in Figure II.1-18. Both curves share the same initial elastic loading during contact initiation; however after the transition into the plastic regime the curve for the normalized stress for the Berkovich indenter is consistently lower than the curve for the conical indenter. There seems to be a geometry effect that is resulting in different indentation responses for the two indenters. It is also

47

observed that the contact stress is approximately 2.5 times the yield stress. This is possible because the constitutive model is shear sensitive and not pressure sensitive.
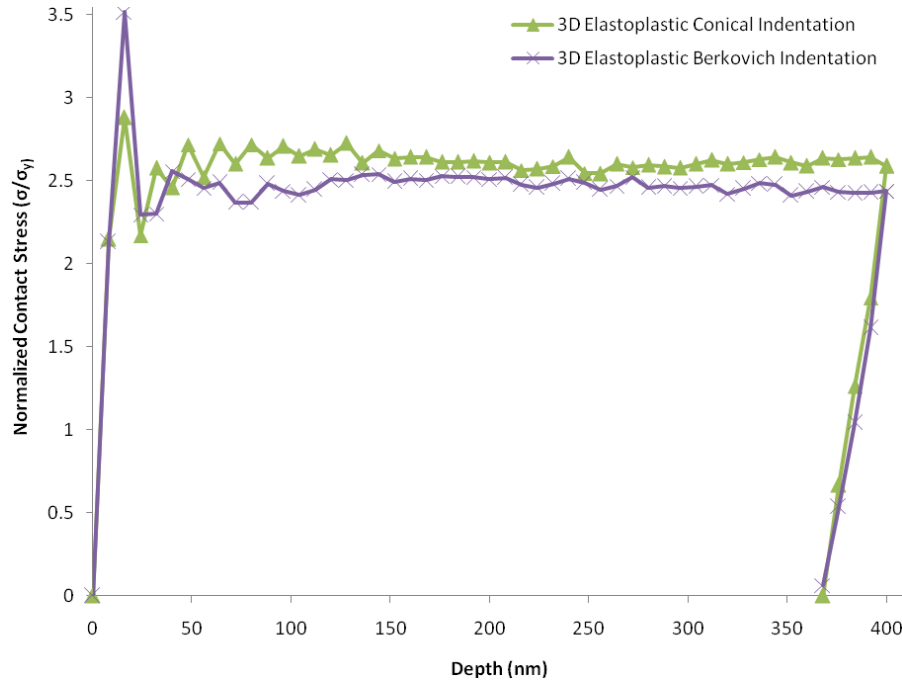
Figure II.1-18: Comparison of normalized contact stresses computed for conical and Berkovich indentation simulations in 6061 aluminum.

To further examine the potential effect of geometry during the elastoplastic indentation, finite element visualizations were utilized to examine the material behavior around the indentation site. Figure II.1-19(a) shows the Mises stress field for the 70.3° conical indenter at maximum indentation depth. The axisymmetric geometry of the conical indenter provides an axisymmetric stress field. Figure II.1-19(b) shows the Mises stress field for the Berkovich indenter with a view cut in the plane perpendicular to a sharp edge of the

48

pyramid which provides an angle similar to that of the equivalent cone. On this cross-section the stress fields between the two indenters are quite similar. Figure II.1-19(c) shows the Mises stress field for the Berkovich indenter with a view cut made in the plane of a sharp edge of the pyramid which provides the cross section with the most dissimilar angle. On this cross-section the stress field extends noticeably further laterally on the side of the flat edge of the pyramid and does not extends as far near the sharper edge.

The distribution of equivalent plastic strain which depends on the material model was also examined. Figure II.1-20(a) shows the equivalent plastic strain distribution on the material surface after conical indentation. The maximum equivalent plastic strain for the conical indentation was 170%. The distribution of equivalent plastic strain for the Berkovich indentation is shown in Figure II.1-20(b). For the Berkovich indentation the maximum equivalent plastic strain was 204% for the same indentation depth as that in conical indentation. It can be seen from the strain distribution that the edges of the pyramid contribute to creating higher equivalent plastic strains in the Berkovich indenter than those experienced by the conical indenter.
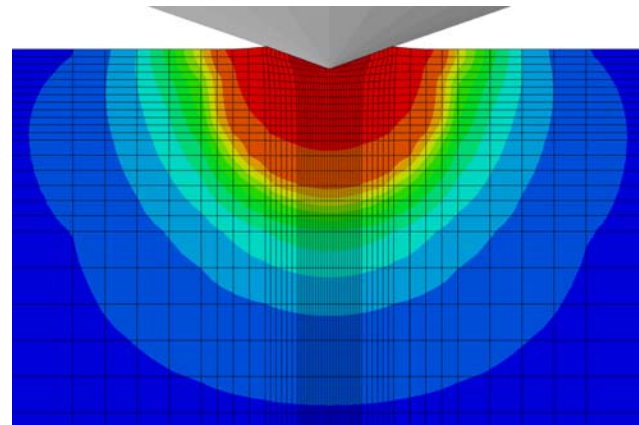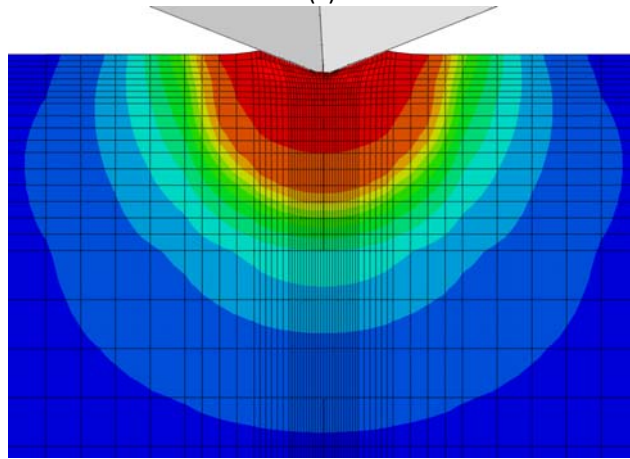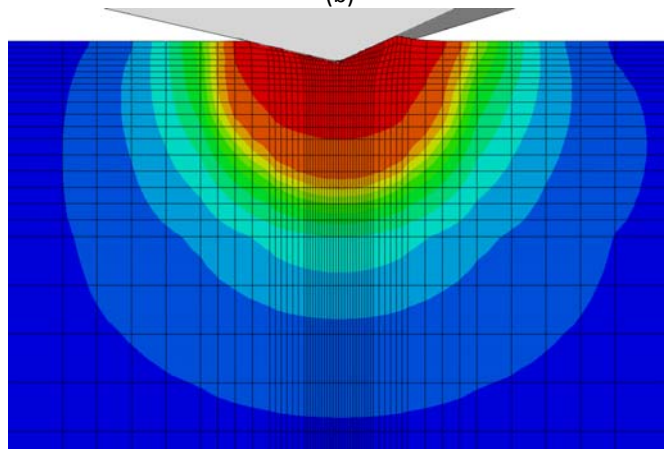
Figure II.1-19: Mises stress in 6061 aluminum for (a) 70.3° conical indenter, (b) Berkovich indenter, viewed in plane perpendicular to indenter edge, and (c) Berkovich indenter, viewed in plane of indenter edge.
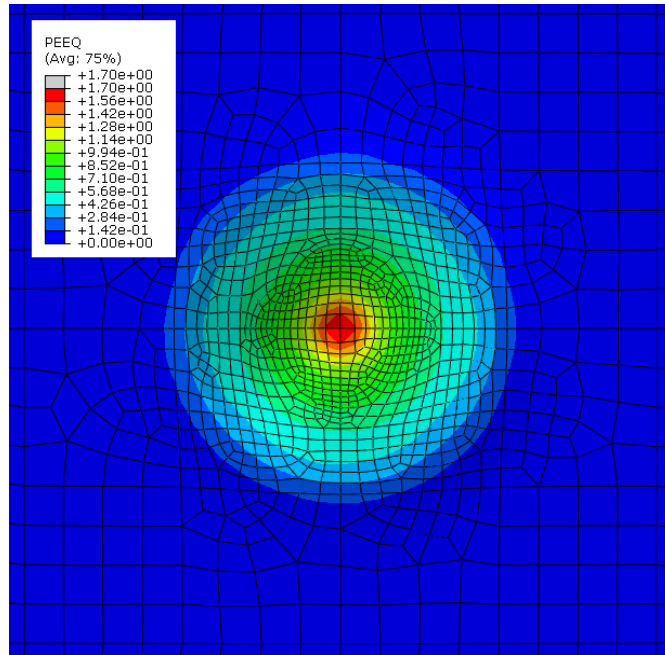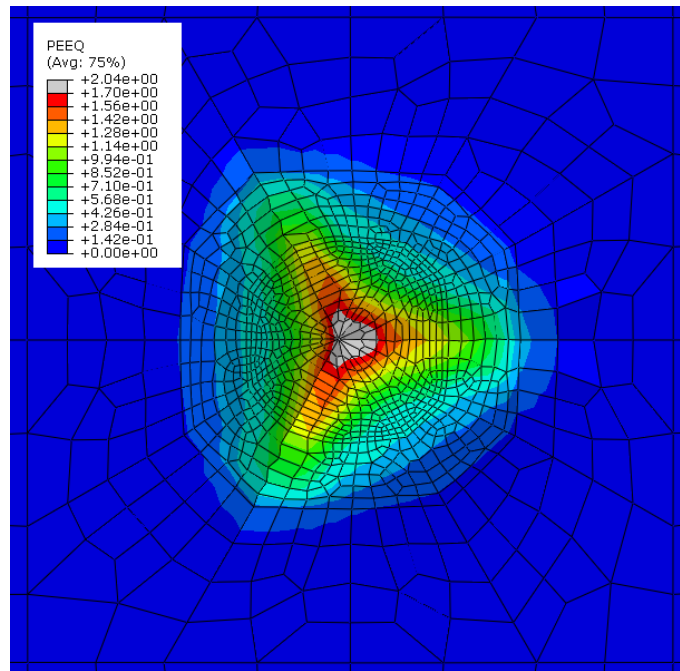
Figure II.1-20: Contours of equivalent plastic strain in 6061 aluminum for (a) 70.3° conical indenter and (b) Berkovich indenter.

51

Despite the contact area being the same throughout the indentation process for both indenters, the material is responding differently due to geometry effects. The edges of the Berkovich pyramidal geometry induce higher plastic strains. This means that for the Berkovich indenter there is more localized yielding in the material. With more localized yielding the material is less resistant to penetration which results in lower required indentation loads for the Berkovich indenter compared to the 70.3° conical indenter.

II.1.5.2 Comparison of Nanoindentation Simulations and Experiments

To assess the validity of numerical simulations, it is always desirable to compare them with the observed responses of the material in nanoindentation experiments. This will also provide additional confidence regarding the ability of the finite element analysis to accurately predict a real nanoindentation test result. Hence, a cylindrical specimen was prepared for the nanoindentation test using the same type of aluminum used in calibration of the finite element model. A series of nanoindentation test were performed using an Asylum Research MFP-3D™ Stand Alone Atomic Force Microscope fitted with a NanoIndenter module (Asylum Research, Santa Barbara, CA). A series of 64 indentations were performed in a grid pattern on the material surface and a sampling of curves showing the variation in load-displacement response among the indentations is shown in Figure II.1-21. The indentations were performed using force control to a maximum indentation force of 1.4mN. The variation in indentation depth is thought to be from variations in the material properties due to the effects of machining the sample. An AFM produced contour

plot of the material surface is shown in Figure II.1-22. The surface roughness for this 100μm2 plot was given as approximately 3.5nm.
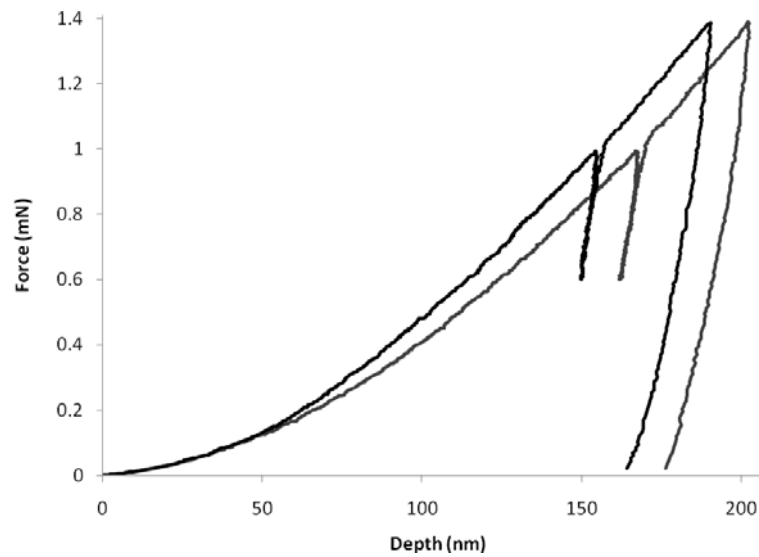
Figure II.1-21: Upper and lower bounds of experimental load–displacement curves in 6061 aluminum.
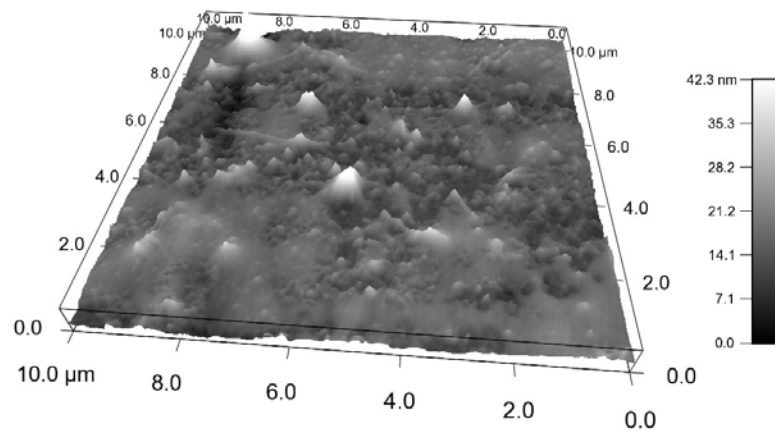
Figure II.1-22: AFM-produced contour plot of 6061 aluminum specimen surface.

Finite element simulations were performed to a maximum depth similar to the experimental indentations. Comparing the unloading slopes of the experimental and simulated curves revealed a Young's modulus from the nanoindentation experiments of approximately 59GPa, which was approximately 9% lower in magnitude than the 65GPa modulus determined in the macro scale test. The simulation results for both the conical and Berkovich indenters provided load-displacement curves with significantly lower loads compared to experimental values. Warren et al. (2006) discuss that machining induced residual stress can significantly affect load-displacement curves. The residual stresses may be estimated through finite element simulation. In their sample of 52100 steel, residual stresses were estimated to be 18% of yield stress in the horizontal direction and 12% of yield stress in the vertical direction. These values were used as a starting point in estimating the residual stresses in the aluminum specimen in the present study.

Using the 2D axisymmetric finite element model (due to its lower computational effort) a series of simulations were performed while adjusting residual stress parameters. The residual stresses were estimated to be approximately 8% of yield stress in the horizontal direction and 5% of yield in the vertical direction. Incorporating these residual stresses as the initial stresses was shown to bring up the computed load-displacement curves well within the experimental bounds. Figure II.1-23 compares the conical and Berkovich indentations without residual stresses, the conical indentation with residual stresses, and the experimental bounds.
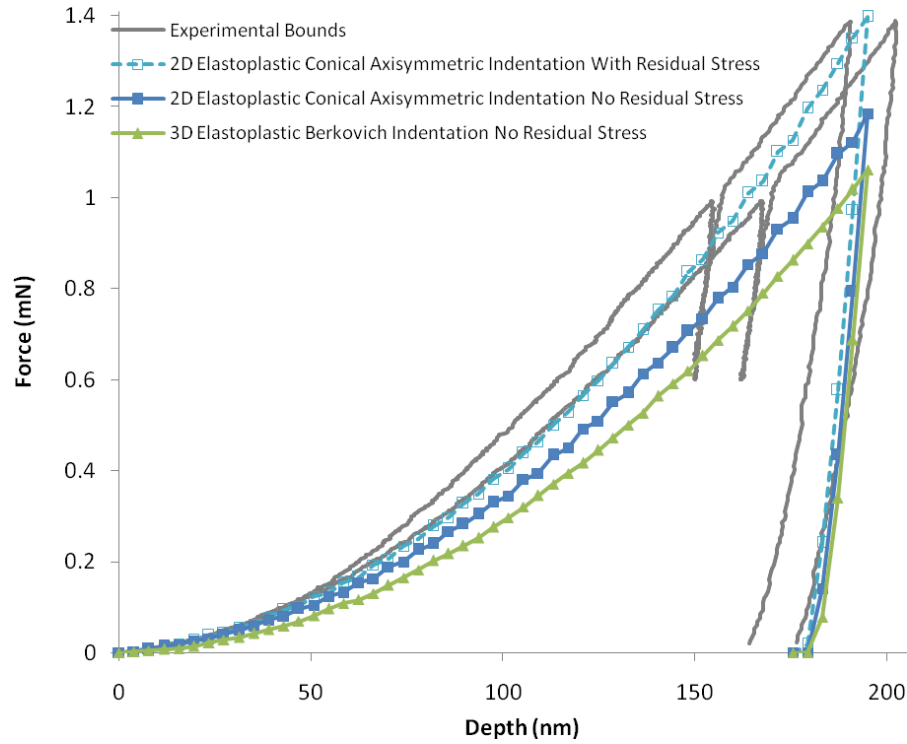
Figure II.1-23: Comparison of numerically obtained force–displacement curves with experimental bounds for 6061 aluminum.

II.1.6 Conclusions

Finite element simulations of elastoplastic nanoindentations were performed for conical (70.3°) and Berkovich indenters to study the effect of indenter geometry on the response of an elastoplastic material. It is shown that there are clear differences in the load-displacement responses between the two indenters. Loads in the Berkovich indentation are noticeably lower. It is confirmed that contact areas during indentation are very similar, resulting in lower normalized contact stress for the Berkovich indenter. Examination of

55

stress fields near the indenter tip shows that the symmetrical cross-sections of the Berkovich indenter are similar to the axisymmetric stress field of the conical indenter and differences arise when compared to asymmetric cross-sections of the Berkovich indenter. Maximum equivalent plastic strain induced by indenter is demonstrated to be 20% higher for the Berkovich indenter. It is concluded that higher localized plastic strains would result in less resistance to indentation by the material and explain the load-displacement behavior. The results reveal that the use of a 70.3° conical indenter to approximate the response from a Berkovich indenter is not valid for all materials.

The ability of finite element analysis to predict experimental nanoindentation results was also examined. Comparisons with experimental results suggest that machining-induced residual stresses have likely affected the experimental results. It is also demonstrated that these residual stresses may be estimated by matching simulated load-displacement curves within the range of experimental curves.

II.2: Nanoindentation in a Viscoelastic Material

II.2.1 Introduction

Nanoindentation in viscoelastic materials presents new challenges due to the time dependent behavior of the material. Thus, the response of the material is sensitive to the speed of penetration by the indenter. With elastic and elastoplastic materials it is common for material parameters such as the elastic modulus to be determined by examining the unloading curve obtained during a nanoindentation test (Oliver, 2004). The techniques are well established and work well for elastic and elastoplastic materials. However, the procedures developed for these materials are either inaccurate or have many uncertainties for viscoelastic materials (VanLandingham, 2001). The time dependence adds complexities to the material behavior that the previous techniques cannot capture. For instance, the Young's modulus of a material is no longer constant like it is with elastic and majority of elastoplastic materials.

There is still much research needed in the investigation of viscoelastic nanoindentation. The use of finite element analysis provides the option to quickly examine the behavior of this type of material by varying key parameters and observing the differences in behavior. The numerical simulations also provide the ability to look more closely at the behavior of a material in nanoindentation. However, for finite element simulations to be useful they must also be proven to accurately predict the behavior observed in experimental nanoindentation curves.

In this study the goal is to examine how well a viscoelastic nanoindentation simulation can capture the behavior of the time dependent material. First it will be confirmed that a

viscoelastic material model can be calibrated given experimental relaxation data. This material response can be defined using Prony series parameters. Then, the study will investigate the nanoindentation response of the viscoelastic material and its comparison to experimental nanoindentation results for the same type of material.

II.2.2 Literature Review

An examination of depth-sensing indentation, as used to measure the elastic modulus of polymeric materials, was performed by VanLandingham et al. (2001). In their paper the authors reviewed the traditional analysis of load-displacement data for nanoindentation and discuss the limitations and uncertainties that are found for various measurements in nanoscale indentation. The authors also discuss that the application of these established methods toward use in polymers often lead to the inaccurate measurements of the elastic modulus. The paper shows that in comparison to bulk measurements obtained in macroscopic experiments the elastic modulus values measured in quasi-static indentations are relatively high. The differences are attributed to the effect of the viscoelastic behavior in the material and its effect on the shape of the load-displacement unloading curve. As a method to potentially alleviate many of the problems associated with the quasi-static indentation testing VanLandingham et al. (2001) discuss the use of dynamic indentation testing. The authors discuss that, previously, rigorous analysis of dynamic indentation behavior of polymers with regard to viscoelasticity has not been reported. The study concludes that for advancements in quantitative characterization of polymer properties there will need to be material-independent calibration procedures, reference materials,

advances in instrumentation, and new analysis and testing procedures to account for polymer viscoelastic behavior (VanLandingham, 2001).

A study by Cheng and Cheng (2005) looks at conical indentation in linear viscoelastic materials and the relationship between contact depth, initial unloading slope, and the viscoelastic properties of the material. In particular they examine the Oliver-Pharr method for determining the contact depth and whether this method is applicable to indentations in viscoelastic materials. In their study the authors use finite element analysis to examine the viscoelastic behavior. The study determines a relationship between initial unloading slope, contact depth, and the instantaneous modulus for a sufficiently high rate of unloading. A relationship between contact depth and indenter displacement is also discussed. From their results the authors conclude that the Oliver-Pharr method of estimating contact depth is not applicable for nanoindentation of viscoelastic materials. These conclusions are based on constant displacement rate loading and are said to hold for other loading conditions (Cheng and Cheng, 2005).

Other studies have also looked into the accuracy of the Oliver-Pharr method to determine material properties of viscoelastic materials. Tranchida et al. (2006) looked into the Oliver-Pharr method's ability to accurately evaluate Young's modulus of polymers by nanoindentation. When comparing Young's modulus determined in macroscopic tests to the modulus determined through the Oliver-Pharr method for a viscoelastic material the study shows that there is clear disagreement between the values. Young's modulus is shown to be overestimated up to 3.3 times by the Oliver-Pharr method. The study proposes

59

the use of a correction factor relating the modulus obtained through nanoindentation and the expected value. The authors conclude that a satisfactory evaluation of the Young's modulus for polymers can be obtained by coupling their correction factor with the calibrations of the Oliver-Pharr method (Tranchida, 2006).

In another study looking further into the issue of using the Oliver-Pharr method for determining Young's modulus, Tranchida et al. (2007) examines the effect of pile-up and viscoelasticity on the overestimation of Young's modulus. The study shows that the effect of pile-up can be minimized by using shallow indentations at a true nanoscale. However, evaluating the Young's modulus with the Oliver-Pharr method still gives rise to significant deviations with respect to the value measured macroscopically. One issue with viscoelastic indentations is the emergence of a "nose" in the unloading force curve. This can be minimized by performing indentation at large loading rates. Again the Young's modulus determined through the Oliver-Pharr method is still concluded to be consistently higher than the bulk elastic modulus. It appears that viscoelasticity has a significant effect on the contact mechanics compared to the elastic one. The conclusion is that the Oliver-Pharr procedure and other methods derived from elastic contact cannot be applied to the load-displacement curve of viscoelastic nanoindentations (Tranchida, 2007).

Nanoindentation is often used in the determining of the material properties in thin films. Zhou and Komvopoulos (2006) examine the viscoelastic behavior of thin films, showing that, with thin films, stiffness increases with the indentation depth due to increased contact area and the effect of the rigid substrate. Thickness and loading rate are discussed

60

as having a strong effect on the films stiffness. Similar to other studies the Oliver-Pharr method of determining Young's modulus overestimates its value though with the thin films the substrate plays a role in the overestimation. The study shows that experimental results for reduced elastic modulus which were modified by subtracting the viscous component show fair agreement with analytical results (Zhou and Komvopoulos, 2006).

Spherical indentation of linear viscoelastic materials are examined in a paper by Ramesh Kumar and Narasimhan (2004). In this study the relaxation response of polymethyl methacrylate (PMMA) determined from a conventional mechanical test. This data from the relaxation response can be used to determine the Prony series which is an exponential series that defines the relaxation function of the material. The study assesses the validity of viscoelastic indentation theories by comparing experimental and finite element indentation results. For spherical indentations the two are shown to be quite similar. The authors show that depth-sensing indentation may be used to extract viscoelastic response function but that the conventional method of using the unloading curve may results in large errors in the determination of Young's modulus (Ramesh Kumar, 2004).

Another study that includes examination of the indentation response of polymethyl methacrylate (PMMA) was performed by Oyen (2006). In the study indentations were performed on PMMA using a Berkovich indenter. It is shown that additional displacements occurred beyond that due to the viscoelastic response. These additional displacements are likely due to plastic deformations and are mainly caused by the sharp edges of the

Berkovich indenter and complicate the viscoelastic analysis. The author states that a spherical indenter may be a better choice to keep the material response within the linear viscoelastic regime. If pyramidal indenter geometry is used then plastic deformations must be considered (Oyen, 2006).

Sane and Knauss (2001) performed a study to determine various material functions of PMMA. The paper presents data for the relaxation response of PMMA which are of particular interest to this thesis. This provides an opportunity to model a second PMMA material, in addition to that reported by Ramesh Kumar and Narasimhan (2004), and provide an opportunity to make a comparison between the indentation responses of two different reported samples of PMMA.

There have been many studies on the response of viscoelastic materials and their response during indentation. There is a clear consensus that conventional method used to determine properties of elastic and elastoplastic materials are not accurate for viscoelastic materials. Further investigation and insights are needed in regards to the response of these materials during nanoindentation.

II.2.3 Material Modeling

II.2.3.1 Description of the Constitutive Model

The viscoelasticity model describes rate-dependent material behavior. These materials experience dissipative losses that are caused by internal damping effects. Considering small

strains, let us assume that that material is subjected to a time varying shear strain, γ(t). The shear stress response, τ(t), is defined as

$$\tau(t) = \int_0^t G_R(t-s)\dot{\gamma}(s)ds \tag{2.1}$$

Where the time dependent shear relaxation modulus, given as $G_R(t)$, characterizes the material response. The constitutive behavior is clearly demonstrated by a relaxation test in which a sudden strain γ is applied to the material specimen and is then held constant. At zero time, taken as when the strain is suddenly applied, the shear stress is given as

$$\tau(t) = G_R(t)\gamma \tag{2.2}$$

Since γ is held constant as a fixed strain, $\dot{\gamma}=0$ for all t>0, after a long period of time the material will converge to a constant stress (Simulia, 2010).

In ABAQUS the material relaxation is defined using the dimensionless form given below:

$$g_R(t) = G_R(t)/G_0 \tag{2.3}$$

The instantaneous shear modulus is $G_0 = G_R(0)$. Given the dimensionless form the equation for shear stress becomes:

$$\tau(t) = G_0 \int_0^t g_R(t-s)\dot{\gamma}(s)ds \tag{2.4}$$

The dimensionless relaxation function $g_R(t)$ then has an initial value of $g_R(0)=1$ and a value at infinity of $g_R(\infty) = G(\infty)/G_0$ (Simulia, 2010).

In ABAQUS, the viscoelastic material is assumed to be defined by a Prony series expansion of the dimensionless relaxation function as follows

$$g_R(t) = 1 - \sum_{i=1}^{N} \overline{g}_i^P (1 - e^{-t/\tau_i^G}) \tag{2.5}$$

Where N, $\overline{g}_i^P$, and τ_i^G are material constants with i=1, 2, …, N. Using Eq. (2.5), the expression for shear stress becomes

$$\tau(t) = G_0(\gamma - \sum_{i=1}^{N} \gamma_i) \tag{2.6}$$

where

$$\gamma_i = \frac{\overline{g}_i^P}{\tau_i^G} \int_0^t e^{-s/\tau_i^G} \gamma(t-s)ds \tag{2.7}$$

The variables γ_i are state variables that control the stress relaxation. The preceding equations are used by ABAQUS to define the time-dependent shear behavior in the viscoelastic model. To obtain the Prony series coefficients ABAQUS can perform a curve fitting viscoelastic material evaluation based on user provided relaxation data, as described in section 2.3.2. A similar method is used for the volumetric response of the system (Simulia, 2010).

II.2.3.2 Calibration of Material Model

The numerical results in this chapter were calibrated by using experimental results found in literature for polymethyl methacrylate (PMMA). All analyses were conducted using ABAQUS (Simulia, 2010). In ABAQUS a viscoelastic material model was used to model the PMMA. Calibration of the material model in ABAQUS requires either the input of relaxation data or a set of Prony series parameters to define the material behavior. For

the viscoelastic simulations presented in this Chapter the material models were calibrated using test data found in literature.

One set of relaxation data was presented by Ramesh Kumar and Narasimhan (2004). The relaxation response in this paper was reported graphically. Hence a number of data points were picked from the reported graphs in order to create a data series representation of the relaxation data. The data was then converted to a dimensionless form for the use in ABAQUS. Table II.2-1 shows the dimensionless data as extrapolated from literature (Ramesh Kumar and Narasimhan, 2004). In addition to the viscoelastic data, an instantaneous Young's modulus of 2600 MPa and a Poisson's ratio of 0.38 are selected based on the information given in the paper.

Table II.2-1: Dimensionless relaxation response.

gR	1	0.823	0.800	0.785	0.773	0.769	0.767	0.763	0.760
Time	0.01	50	100	150	200	250	300	400	1000

Viscoelastic material response can be defined through a Prony series representation. ABAQUS allows for evaluation of viscoelastic material behavior using the dimensionless relaxation test data. During the material evaluation, ABAQUS performs a curve fitting to the test data and upon completion displays the Prony series parameters and material response for standard relaxation and creep tests. The Prony series parameters calculated by

ABAQUS for the Ramesh Kumar and Narasimhan relaxation data are shown in Table II.2-2.

Table II.2-2: Two-term Prony series from material analysis.

i	g(i) Prony	k(i) Prony	τ(i)
1	0.14366	0	11.346
2	9.83E-02	0	115.69

The material model calibration was performed through a simulation using a single finite element subjected to a uniaxial displacement to create a 1% strain with the viscoelastic material model defined using the aforementioned Prony series parameters. Using the stress data and the relation $\sigma(t)=G(t)\varepsilon_0$ the relaxation response for the ABAQUS model was determined. A comparison between the viscoelastic model simulation and the experimental data presented by Ramesh Kumar and Narasimhan is shown in Figure II.2-1.
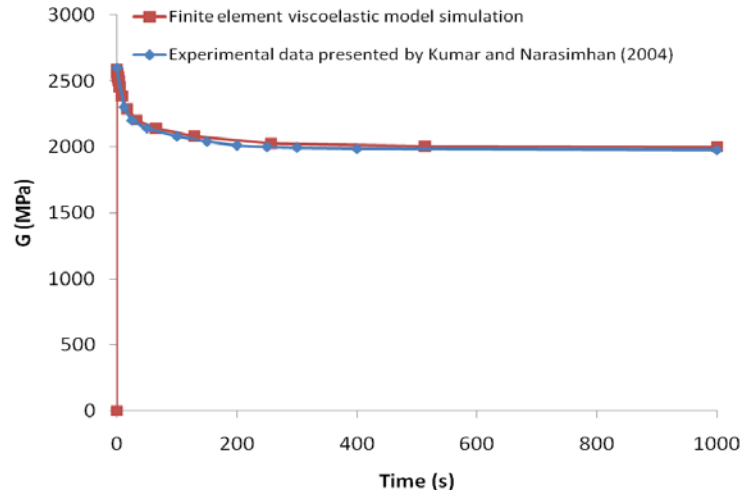
Figure II.2-1: Comparison of experimental relaxation response to viscoelastic finite element simulation for PMMA.

The ABAQUS simulation exhibited good agreement with the experimental values, with only slight differences noticeable throughout the response. With the simulation agreeing with the values reported in literature the model was determined to be well calibrated.

II.2.4 Finite Element Modeling

The finite element nanoindentation models in this chapter were investigated using ABAQUS. The models used are 2D axisymmetric models using either spherical or conical indenters. 2D axisymmetric models have the advantage of allowing quicker simulations than equivalent 3D models.

II.2.4.1 Verification of the Finite Element Model

A viscoelastic material model of polymethyl methacrylate (PMMA) was calibrated from relaxation data reported by Ramesh Kumar and Narasimhan (2004) as described

67

earlier in the thesis. Ramesh Kumar and Narasimhan also present results for spherical indentation. To verify the 2D axisymmetric indentation model using ABAQUS, a spherical indentation simulation was used to recreate the results presented by Ramesh Kumar and Narasimhan.

The spherical indentation model was created by using the axisymmetric model from the previous chapter and adapting it to include a spherical indenter. The indenter was sized to a radius of 3.5mm to match that of the experiment presented in Ramesh Kumar and Narasimhan (2004) and the specimen was sized to 17.5mm on each side. The specimen was modeled as a viscoelastic isotropic deformable solid with elastic parameters set to an instantaneous E=2600MPa, ν=0.38, and viscoelastic behavior defined by the Prony series parameters as shown in Table II.2-2. The indenter was modeled as an elastic isotropic deformable solid with an elastic modulus large enough to prevent deformation of the indenter during indentation. The indentation simulation used load control with a triangular load history with a rise time of 10s and a maximum load of 100N. Contact between the indenter and specimen was modeled as frictionless. The finite element mesh with indenter is shown in Figure II.2-2.
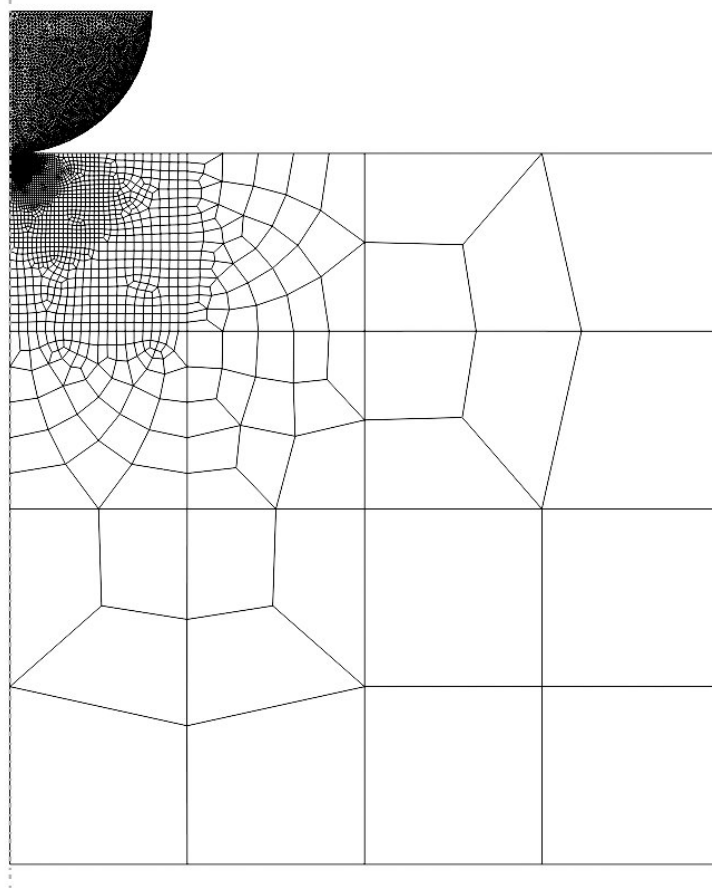
Figure II.2-2: Finite element mesh with indenter used for spherical indentation.

A viscoelastic finite element analysis was performed on the above described model. From the simulation the load and displacement values were recorded for a direct comparison with the results presented in Ramesh Kumar and Narasimhan (2004). Two different figures were used for comparison.

The first figure used in the comparison is a displacement-time history plot. The experimental results extrapolated from Ramesh Kumar and Narasimhan (2004) are compared with finite element results from ABAQUS and are shown in Figure II.2-3. The

two plots were in excellent agreement for a large range of the indentation process. There was some slight deviation during the unloading portion of the plot where the finite element simulation experiences displacements were slightly lower than the experimental data.

Figure II.2-3: Comparison of simulated and experimental spherical indentation displacement-time responses for PMMA.

A comparison of the load-displacement response was also performed. The curves for the experimental and finite element load-displacement results are show in Figure II.2-4. In this figure the differences between the curves become more noticeable. There were some differences in both the loading and unloading portions of the curves. The differences during loading were mostly during the initial stage of the loading of load under 20N, with the

70

loads from the experiment being slightly higher. During unloading the behavior was still similar but there were some more pronounced differences. Particularly the recovery of the material in the experiment seems to lag behind the response of the finite element simulation. The latter difference is probably due to a slight elastoplastic behavior in the material.
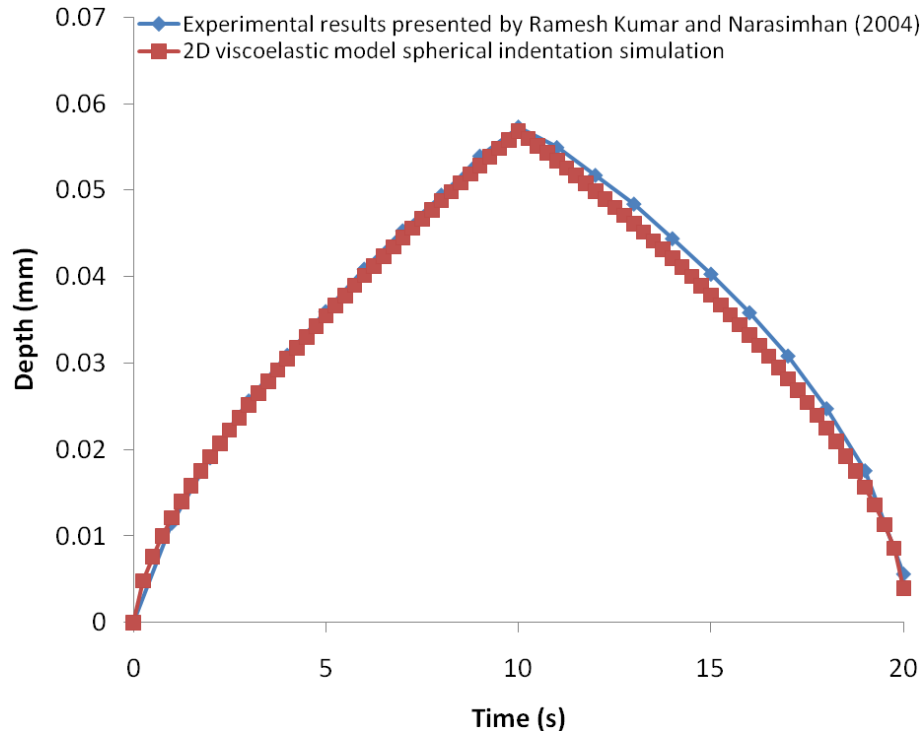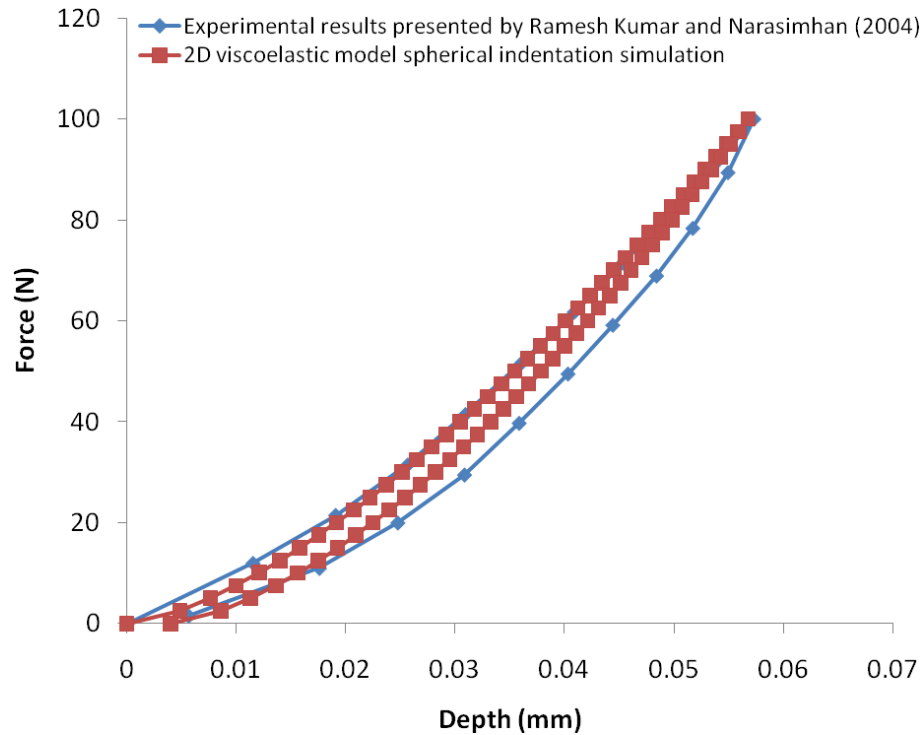

Figure II.2-4: Comparison of simulated and experimental spherical indentation load-displacement responses for PMMA.

In the paper by Ramesh Kumar and Narasimhan (2004) the experimental results were similarly compared to numerical and analytical results for the indentation. The comparisons

71

performed in this thesis compare well to those presented before and similar differences were observed between experimental and numerical results. The simulations presented here then show good verification of the finite element model.

II.2.5 Results and Discussion

It has been shown by Ramesh Kumar and Narasimhan (2004) and Tranchida et al. (2007) that obtaining viscoelastic material parameters from nanoindentation plots with the conventional methods used for elastic and elastoplastic materials has many inaccuracies. Using the Prony series parameters shown in Table II.2-2 as a starting point, an investigation was performed to see whether experimental nanoindentation results on a sample of polymethyl methacrylate (PMMA) as presented in a different study could be matched through adjustment of the Prony series parameters.

A study that provided load-displacement results from nanoindentation on PMMA was presented by Oyen (2006). The nanoindentations reported by Oyen were performed by using a Berkovich indenter and a triangular load history to a maximum indentation load of 10mN. The experiments used for comparison had a rise time of 500s. To perform the finite element simulation of the nanoindentation a 2D axisymmetric model using an equivalent 70.3° conical indenter was used. A 2D model was chosen due to its lower computational requirements allowing for more iterations of the simulation in a shorter time frame.

After running an initial finite element analysis of the nanoindentation using the same loading history as presented by Oyen (2006) the simulation and documented experimental results were compared. This comparison is shown in Figure II.2-5. The two response curves were in good agreement through the loading portion of the indentation, with only slight differences being noticeable. However, during the unloading phase of the indentation the responses differed significantly. The experiment shows a significant amount of residual

depth after the completion of the test, whereas in the simulation the residual depth was fairly minimal.
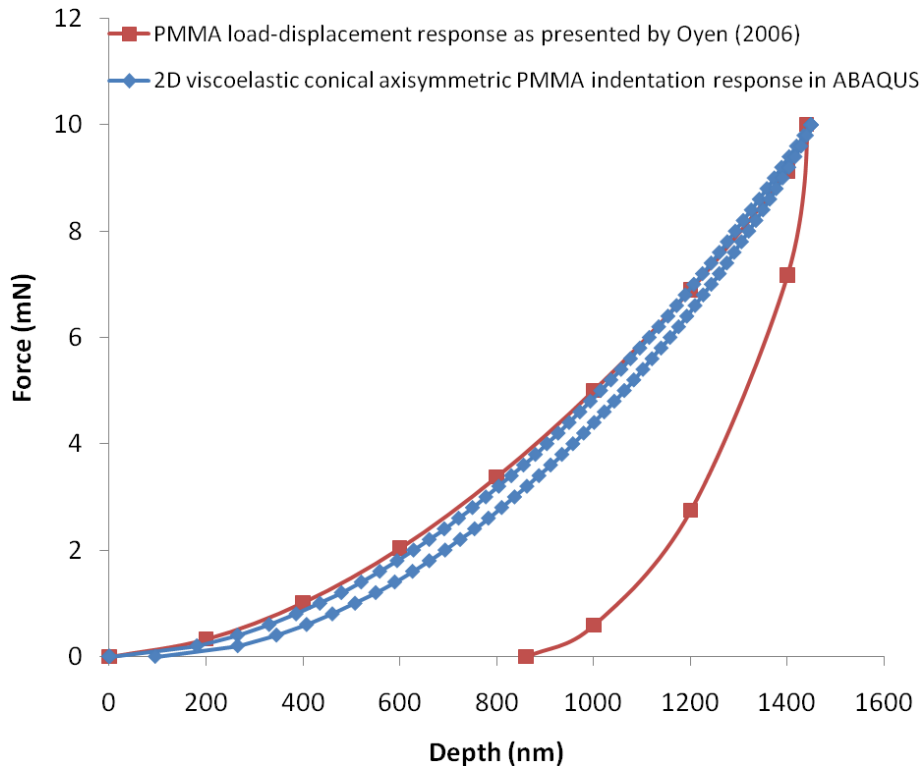
Figure II.2-5: Comparison of load-displacement responses of PMMA obtained from finite element simulation against the experimental data by Oyen (2006). Material model parameters are calibrated from Ramesh Kumar and Narasimhan (2004) data.

The simulation seemed to do a good job of predicting the loading response during the indentation; however the unloading response did not provide a good prediction of the experimental behavior. These differences could have been due to the differences in morphology between the PMMA specimens used in the two studies and/or due to the

effects of the sharp Berkovich indenter used in obtaining the experimental response. Using the calibrated response as a starting point, an investigation into the effect of adjusting the Prony series parameters was performed.

In order to get an understanding of how different Prony series parameters adjustments would affect the load-displacement response in a nanoindentation test a sensitivity study was performed. For the sensitivity study a single parameter was adjusted at a time and the change in the shape of the response curve was noted. Adjustments were made using a two-term Prony series so that adjustments could be compared to the calibrated response.
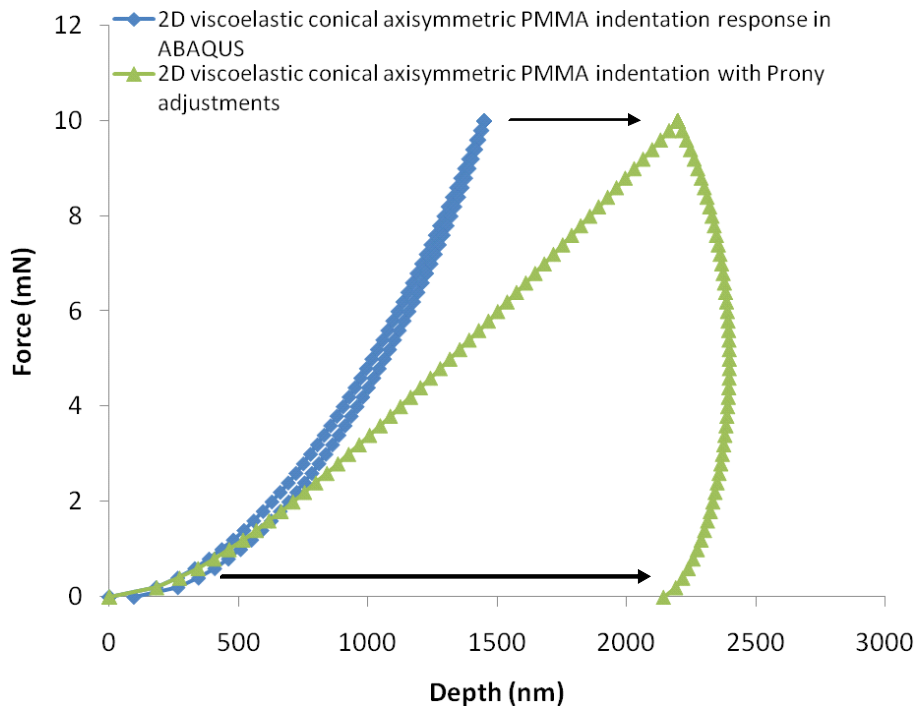

Figure II.2-6: Change in simulation response after an increase in the g(2) term.

75

The first adjustment was made to the g(2) term. The value was adjusted from 0.0983 to 0.8. The simulation result from this single adjustment is shown in Figure II.2-6. The figure shows that this adjustment produces a very significant increase in both the maximum indentation depth from the 10mN force as well as the residual displacement after unloading.

An adjustment was then made to the $\tau(2)$ term in the Prony series. The term was adjusted from the original value of 115.69 to 500. The difference in the simulation is shown in Figure II.2-7. This figure shows that this adjustment has the effect of decreasing the maximum indentation depth. The two parameters have opposing effects in how they affect the simulation response. It was thought then that adjustments to both parameters could provide a material response where the maximum indentation depth remains the same but the residual displacement after indentation has increased. A series of simulations were then performed making adjustments to both parameters to test this.
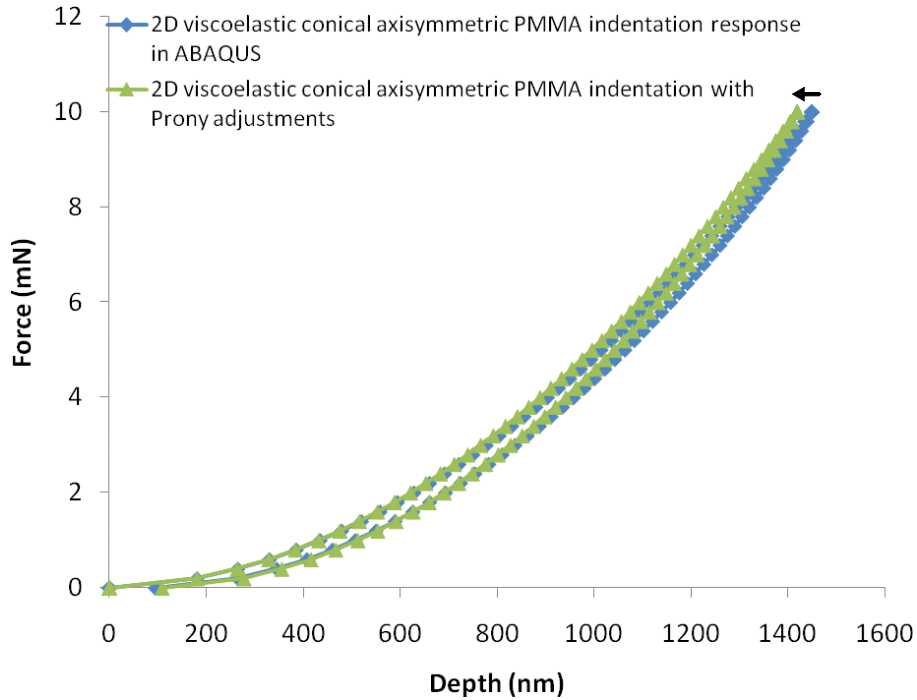
Figure II.2-7: Change in simulation response after an increase in the τ(2) term.

Through the series of simulations a new finite element response was obtained that was closer to the experimental curve. Since making adjustments to increase the residual displacement also had the effect of increasing the maximum displacement at peak load, it was difficult to maintain the same initial loading behavior which matched well from the initial calibrated simulation. Adjustments were ultimately made to both terms of the Prony series and the final term values were; g(1)=0.11, τ(1)=100, g(2)=0.3, τ(2)=200. The response using these parameter adjustments is shown in Figure II.2-8. As the figure shows the loading response maintained good agreement with the original calibrated simulation and the experimental results, however, the maximum displacement had increased slightly.

The residual displacement had increased in the new simulation to account for 50% of that in the experimental data.
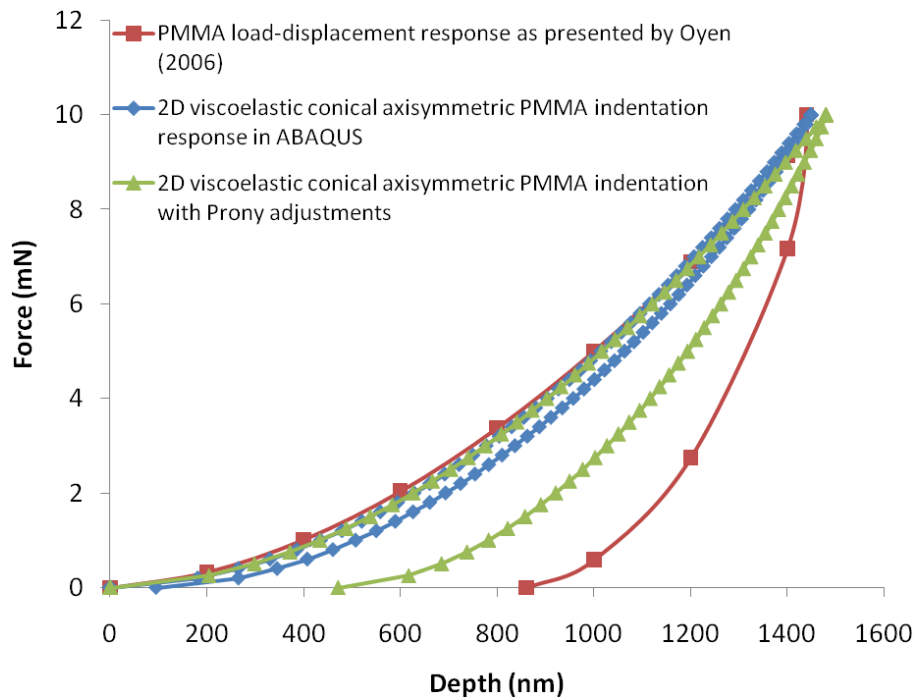
Figure II.2-8: Comparison of simulation before and after Prony adjustments to experimental Berkovich nanoindentation load-displacement response by Oyen (2006) for PMMA.

It was shown that adjusting Prony series parameters to affect the shape of the simulated load-displacement curve to more closely match an experimental curve was possible. However, the adjustments seemed to have a limit to how much they could be adjusted while maintaining the behavior that was already in good agreement.

After the parametric study, a different relaxation response of PMMA as reported in a paper by Sane and Knauss (2001) was examined for its response in nanoindentation. Similar to before, data points were taken from a relaxation response figure and the data series was used to define a viscoelastic material. A material analysis in ABAQUS revealed that this material was defined by a six-term Prony series. Figure II.2-9 shows the indentation response of the material in comparison to the simulation response from the Prony series parameter study and the experimental indentation curve from Oyen (2006). The loading response of all considered simulations and the experimental data were in good agreement. Interestingly, the simulated response of the PMMA presented by Sane and Knauss (2001) was very similar to the response obtained in the Prony series parametric study, except for some slight deviation during the latter half of the unloading phase.

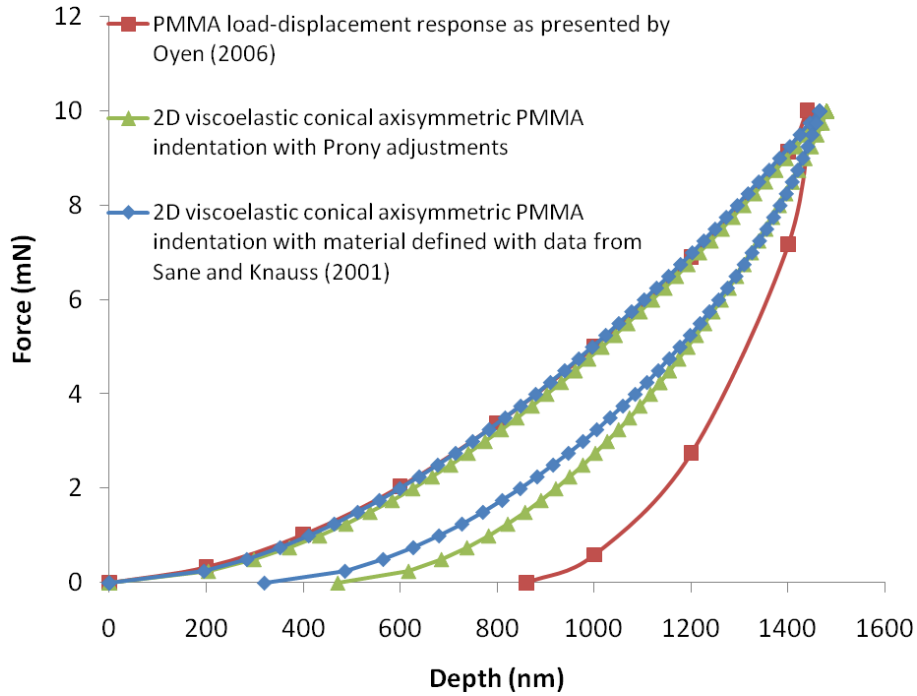Figure II.2-9: Comparison of simulations from Prony series adjustments and that calibrated from Sane and Knauss (2001) data to experimental Berkovich nanoindentation load-displacement response for PMMA.

The similarities in response from the Prony series parametric study simulation and the simulation calibrated from the data in Sane and Knauss (2001) provided motivation to look into the relaxation responses of the finite element models used in this study. The relaxation response was attained through finite element simulation as described earlier in this thesis. A comparison of the finite element analysis results for the relaxation responses of the calibrated Ramesh Kumar and Narasimhan (2004) and Sane and Knauss (2001) models as well as the model developed through the Prony parameter study are shown in Figure II.2-10. The comparison shows that the relaxation response for the Sane and Knauss data is well predicted by the model developed through the Prony series parametric study. This showed

80

that it is possible to predict different morphology responses for the same type of polymer

through Prony series parameter adjustment.
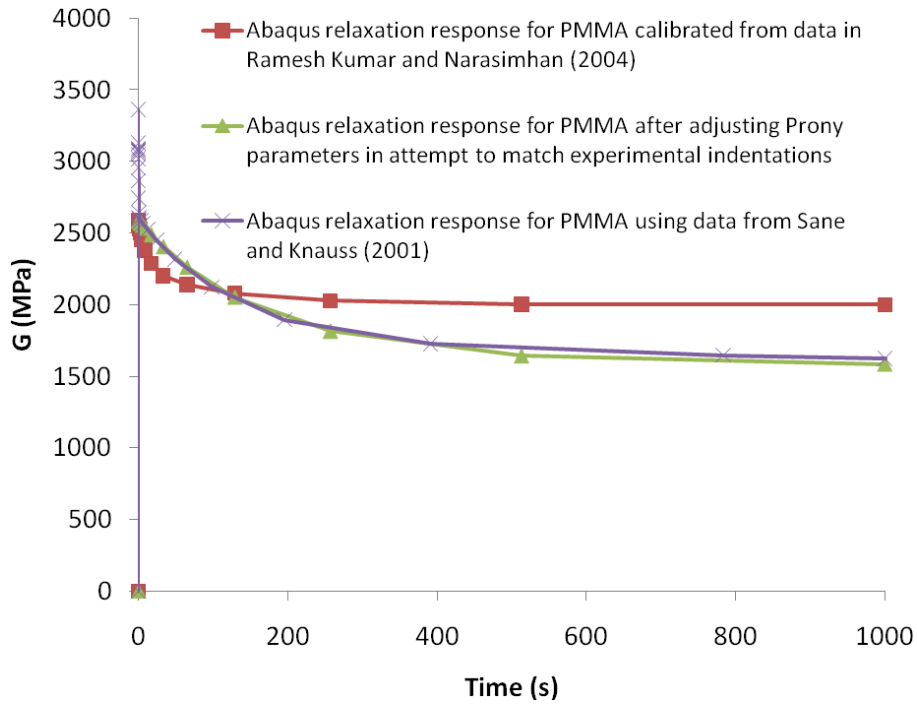
Figure II.2-10: Comparison of relaxation responses of PMMA for simulations using Prony

adjustments, calibrated from Sane and Knauss (2001) data, and calibrated from Ramesh

Kumar and Narasimhan (2004) data.

After adjusting Prony series parameters in an attempt to simulate an experimental

nanoindentation response through numerical analysis it seemed that there was a limit to the

extent of the manipulation. The adjusted model had a response closer to the experimental

curve but there was still a significant difference during unloading. However, the adjusted

model did match well with the simulation of another model calibrated from an

experimental relaxation response found in literature. It is possible that for the prediction of the experimental nanoindentation curves a more complex Prony series defined by more terms would be needed. However, it seems more likely that the additional residual deformation during unloading is due to the onset of plastic deformation due to effects from the sharp pyramidal indenter.

II.2.6 Conclusions

A finite element model was calibrated for polymethyl methacrylate (PMMA) using relaxation data reported in literature. The model displayed good agreement with the reported relaxation and spherical indentation responses. The nanoindentation response of the finite element model using a Berkovich equivalent conical indenter was then compared to experimental results reported in literature using a Berkovich indenter. The comparison showed good agreement in the loading response. However, the unloading response for the experimental curve displayed a greater amount of residual displacement than shown in the numerical result.

Prony series parameters for the calibrated model were calculated by evaluating the material in ABAQUS. A series of Prony parameters adjustments were performed in an effort to more closely match the numerical solution to the experimental nanoindentation result. The resulting adjusted model had a response more similar to the experimental result but still had a smaller residual displacement during unloading. It was found however that this adjusted model provided a similar response to a finite element model calibrated with other PMMA relaxation data reported in literature.

The results show that it is possible to provide predictions for different samples of PMMA through Prony series parametric studies. However, there are still issues in regard to providing predictions of Berkovich indenter nanoindentation. The residual displacements experienced in the experimental indentation are thought to be from plastic deformations caused by the sharp pyramidal geometry of the Berkovich indenter.

II.3: Conclusions and Future Challenges

Elastoplastic nanoindentations using conical (70.3°) and Berkovich indenters were investigated using finite element simulations to study the effect of indenter geometry on the response of the material. The simulations show clear differences in the load-displacement responses of two indenters. Loads in the Berkovich indentation are noticeably lower even though the contact areas during indentation are very similar. The result was lower normalized contact stress for the Berkovich indenter. Examination of stress fields near the indenter tip showed that maximum equivalent plastic strain induced by indenter is 20% higher for the Berkovich indenter. The higher localized plastic strains would result in less resistance to indentation by the material and explain the load-displacement behavior. The results reveal that the use of a 70.3° conical indenter to approximate the response from a Berkovich indenter is not valid for all materials.

The ability of finite element analysis to predict experimental nanoindentation results was also examined. Comparisons suggest that machining-induced residual stresses have likely affected the experimental results. Residual stresses may be estimated by matching simulated load-displacement curves within the range of experimental curves.

Finite element analysis of viscoelastic material was also examined. Using relaxation data reported in literature a finite element model was calibrated for polymethyl methacrylate (PMMA). Simulations of a relaxation and spherical indentation tests displayed good agreement with the reported curves. Nanoindentation analysis using a

Berkovich equivalent conical indenter showed good agreement in the loading response compared to reported experimental curves using a Berkovich indenter. However, the unloading response displayed a greater amount of residual displacement in the experimental results.

A Prony parameter adjustment study was performed in an effort to more closely match the numerical solution to the experimental nanoindentation result. The adjusted model had a response more similar to the experimental result but still had a smaller residual displacement during unloading. However, the adjusted model provided a similar response to a finite element model calibrated with different PMMA relaxation data reported in literature.

It was shown to be possible to provide predictions for different samples of PMMA through Prony series parametric studies. Conversely, there are challenges in providing predictions of Berkovich indenter nanoindentation. The residual displacements in the experimental indentation are considered to be from plastic deformations caused by the sharp pyramidal geometry of the Berkovich indenter.

Insights have been gained into the behavior of elastoplastic and viscoelastic materials during nanoindentation. Nevertheless, there are many questions that remain in the areas of numerical and experimental nanoindentation. This thesis has explored the comparison of conical and Berkovich indenters through simulation. The examination of additional materials following various hardening laws is still needed. In addition, investigations into the comparison of the two "equivalent" tip geometries through experimental

nanoindentations in different materials would provide valuable information into the equivalence assumption.

In the viscoelastic comparisons, plastic deformation effects were observed in the experimental indentations. Further work examining the effect of plastic deformation in polymer indentations is needed. Methods for developing a finite element viscoplasticity model based on experimental nanoindentation curves would be particularly valuable.

The methods used for the examination of material behavior in nanoindentation have been extensively developed since the inception of the technique. The methods work well for many types of materials and for different indenter types. Modern nanoindenters and finite element software are making examination of these problems more accessible. However, there are still many challenges that remain for the examination of more complex material types and how they will respond to different indenter geometries.

II.4 References

ABAQUS Analysis User's Manual. Version 6.9, Dassault Systèmes, Simulia, 2010.

Cheng, Y.-T., and Cheng, C.-M., 2005, "Modeling Indentation in Linear Viscoelastic Solids", R11.2, *Fundamentals of Nanoindentation and Nanotribology III. Materials Research Society Symposium Proceedings*, Wahl, K.J., Huber, N., Mann, A.B., Bahr, D.F., and Cheng, Y.-T., eds., Warrendale, PA, **841**.

Huang, G., and Lu, H., 2007, "Measurements of Two Independent Viscoelastic Functions by Nanoindentation", *Experimental Mechanics*, **47**, pp. 87-98.

Knapp, J.A., Follstaedt, D.M., Myers, S.M., Barbour, J.C., and Friedmann, T.A., 1999, "Finite-element modeling of nanoindentation", *Journal of Applied Physics*, **85**(3), pp. 1460-1474.

Li, M., Chen, W.M., Liang, N.G., and Wang, L.D., 2004, "A numerical study of indentation using indenters of different geometry", *Journal of Materials Research*, **19**(1), pp. 73-78.

Mencik, J., 2007, "Determination of mechanical properties by instrumented indentation", *Meccanica*, **42**, pp. 19-29.

Moore, S.W., Manzari, M.T., and Shen, Y., 2010, "Nanoindentation in elastoplastic materials: insights from numerical simulations", *International Journal of Smart and Nano Materials*, **1**(2), pp. 95-114.

Oliver, W.C. and Pharr, G.M., 2004, "Measurements of hardness and elastic modulus by instrumented indentation: Advances in understanding and refinements to methodology", *Journal of Materials Research*, **19**(1), pp. 3-20.

Oyen, M.L., 2006, "Analytical Techniques for Indentation of Viscoelastic Materials", *Philosophical Magazine*, **86**(33-35), pp. 5625-5641.

Panich, N., Kraivichien, V., and Yong S., 2004, "Finite element simulation of nano-indentation of bulk materials", *Journal of Scientific Research of Chulalongkorn University*, **29**(2), pp. 145-153.

Pelletier, H., Krier, J., Cornet, A., and Mille, P., 2000, "Limits of using bilinear stress-strain curve for finite element modeling of nanoindentation response of bulk materials", *Thin Solid Films* **379**, pp. 147-155.

Poon, B., 2009, "A critical appraisal of nanoindentation with application to elastic-plastic solids and soft materials", Ph.D. dissertation, California Institute of Technology.

Ramesh Kumar, M.V., and Narasimhan, R., 2004, "Analysis of Spherical Indentation of Linear Viscoelastic Materials", *Current Science*, **87**(8), pp. 1088-1095.

Roylance, D., 2001, "Engineering Viscoelasticity", Department of Materials Science and Engineering, Massachusetts Institute of Technology, Cambridge.

Sakhorova, N.A., Fernandes, J.V., Antunes, J.M., and Oliveira, M.C., 2009, "Comparison between Berkovich, Vickers and conical indentation tests: A three-dimensional numerical simulation study", *International Journal of Solids and Structures*, **46**, pp. 1095-1104.

Sane, S.B., and Knauss, W.G., 2001, "On Interconversion of Various Material Functions of PMMA", *Mechanics of Time-Dependent Materials*, **5**, pp. 325-343.

Swaddiwudhipong, S., Hua, J., Tho, K.K., and Liu, Z.S., 2006, "Equivalency of Berkovich and conical load-indentation curves", *Modelling and Simulation in Materials Science and Engineering*, **14**, pp. 71-82.

Tranchida, D., Piccarolo, S., Loos, J., and Alexeev, A., 2006, "Accurately Evaluating Young's Modulus of Polymers through Nanoindentations: A Phrenomenological Correction Factor to the Oliver and Pharr Procedure", *Applied Physics Letters*, **89**, 171905.

Tranchida, D., Piccarolo, S., Loos, J., and Alexeev, A., 2007, "Mechanical Characterization of Polymers on a Nanometer Scale through Nanoindentation. A Study of Pile-up and Viscoelasticity", *Macromolecules*, **40**(4), pp. 1259-1267.

VanLandingham, M.R., Chang, N.-K., Drzal, P.L., White, C.C., and Chang, S.-H., 2005, "Viscoelastic Characterization of Polymers Using Instrumented Indentation. I. Quasi-Static Testing", *Journal of Polymer Science: Part B: Polymer Physics*, **43**, pp. 1794-1811.

VanLandingham, M.R., Villarrubia, J.S., Guthrie, W.F., and Meyers, G.F., 2001, "Nanoindentation of Polymers: An Overview", *Recent Advances in Scanning Probe Microscopy. Proceedings. 220th American Chemical Society National Meeting*, Tsukruk, V. V. and Spencer, N. D., eds., Wiley-VCH Verlag GmbH, Washington, DC, pp. 15-43.

Wang, F., and Keer, L.M., 2005 "Numerical simulation for three dimensional elastic-plastic contact with hardening behavior", *Journal of Tribology*, **127**(3), pp. 494-502.

Warren, A.W., and Guo, Y.B., 2006, "Machined surface properties determined by nanoindentation: Experimental and FAE studies on the effects of surface integrity and tip geometry", *Surface & Coatings Technology*, **201**, pp. 423-433.

Xu, Z., and Li, X., 2008 "Effects of indenter geometry and material properties on the correction factor of Sneddon's relationship for nanoindentation of elastic and elastic-plastic materials", Acta Materialia **56**, pp. 1399-1405.

Zhou, J., and Komvopoulos, K., 2006, "Surface and Interface Viscoelastic Behaviors of Thin Polymer Films Investigated by Nanoindentation", *Journal of Applied Physics*, **100**,114329.